AGU
ADVANCING EARTH AND SPACE SCIENCES

JGR Planets

Key Points:

- The predicted mantle mineralogy in sub-Earths and Mercury-sized exoplanets includes pyroxenes, olivine, garnet, and silica polymorphs
- Five different meteorites have been chosen as precursor materials to model the rocky mantle, belonging to CH, CB, EN, and aubrite groups
- A pyroxene-rich mantle shows different chemical and physical properties, affecting exo-Mercuries' internal structures and their evolution

Author Contributions:

Conceptualization: Camilla Cioria, Giuseppe Mitri
Funding acquisition: Giuseppe Mitri
Investigation: Camilla Cioria
Methodology: Camilla Cioria, James Alexander Denis Connolly
Project administration: Giuseppe Mitri
Software: James Alexander Denis Connolly
Supervision: Giuseppe Mitri, Jean-Philippe Perrillat
Writing – original draft: Camilla Cioria, Giuseppe Mitri, Jean-Philippe Perrillat, Fabrizio Saracino
Writing – review & editing: Camilla Cioria, Giuseppe Mitri

Mantle Mineralogy of Reduced Sub-Earths Exoplanets and Exo-Mercuries

Camilla Cioria[1,2] , Giuseppe Mitri[1,2], James Alexander Denis Connolly[3] , Jean-Philippe Perrillat[4] , and Fabrizio Saracino[5]

[1]International Research School of Planetary Sciences, Università d'Annunzio, Pescara, Italy, [2]Dipartimento di Ingegneria e Geologia, Università d'Annunzio, Pescara, Italy, [3]Department of Earth Sciences, Institute for Geochemistry and Petrology, ETH Zürich, Zürich, Switzerland, [4]Laboratoire de Géologie de Lyon, CNRS, Université de Lyon, Université Lyon 1, Ens de Lyon, Villeurbanne, France, [5]Department of Geology, University of Liège, Liège, Belgium

Abstract The mineralogy of planetary mantles formed under reducing conditions, as documented in the inner regions of the solar system, is not well constrained. We present thermodynamic models of mineral assemblages that would constitute the mantles of exo-Mercuries. We investigated reduced materials such as enstatite chondrites, CH, and CB chondrites, and aubrites, as precursor bulk compositions in phase equilibrium modeling. The resulting isochemical phase diagram sections indicate that dominant phases in these reduced mantles would be pyroxenes rather than olivine, contrasting with the olivine-rich mantles found within Earth, Mars, and Venus. The pyroxene abundances in the modeled mantles assemblages depend on the silica content shown by precursor materials. The silica abundance in the mantle is closely related to Si abundance in the core, particularly in reduced environments. In addition, we propose that pyroxene-rich mantles exhibit more vigorous convective and tectonic activity than olivine-rich mantles, given that pyroxene-rich mantles would have lower viscosity and a lower solidus temperature (Ts).

Plain Language Summary Mineral assemblages that constitute the mantles of reduced exoplanets, such as those formed in the inner regions of stellar nebulae, have been scarcely investigated. We propose that these exoplanets share several physical and chemical properties with planet Mercury in our Solar System, as they formed in a similar geochemical environment. In order to outline the minerals constituting these mantles, we take in account all the chemical compositions previously proposed to match Mercury's observed characteristics. These compositions are extrapolated from several classes of meteorites, among the most pristine materials currently known and best candidates as "building blocks" of planetary objects. We, then use the well-established thermodynamic code Perple_X to predict the stable minerals at pressure and temperature ranges assumed for these exoplanets' interiors. We find that silicate mantles of exoplanets located in inner regions of nebulae are dominated by pyroxene group minerals, rather than olivine, as in the Earth's mantle. This results in different rheological (e.g., viscosity) and physical properties (e.g., melting behavior) for these reduced exoplanets, with significant implications for their mantle dynamics and evolution over time.

1. Introduction

Since the first detections of exoplanets orbiting neutron stars (Wolszczan & Frail, 1992) and Sun-like stars (Marcy & Butler, 1996), thousands of exoplanets have been discovered, especially through the techniques of Doppler spectroscopy and transit photometry. The *Kepler* space telescope (Batalha et al., 2011, 2013) discovered more than 134 exoplanets, with a wide range of physical properties. Many of them exhibit a rocky nature, with surfaces, dominated by silicates.

Recently, several studies have attempted to model the internal structure of super-Earths-planetary bodies having masses between 1 and 10 M_E-focusing on phase transitions among ultrahigh-pressure minerals (Boujibar et al., 2020; Duffy et al., 2015; Sotin et al., 2010; Stixrude, 2014; Umemoto et al., 2006, 2017; Valencia, 2013; Valencia et al., 2006). Boujibar et al. (2020) described an up to five-layered mantle, where the dominant mineral phases would be olivine and perovskite supergroup members, similar to Earth's mantle mineralogy. Putirka and Rarick (2019) offered a comprehensive estimation of the range of exoplanets mineralogy using stellar compositions from the Hypatia Catalog (Hinkel et al., 2014, 2016), highlighting the important role of Fe partitioning during core formation in determining the dominance of olivine and/or orthopyroxene in exoplanetary mantles.

Several efforts have been made to describe the metal-silicate partitioning and core formation processes in super-Earths and larger rocky exoplanets (e.g., Schaefer et al., 2017; R. F. Smith et al., 2018; Wicks et al., 2018).

Our understanding of the composition and internal structure of exoplanets with sizes comparable to Earth and Mercury is currently limited, due to observational biases that favor the detection of larger exoplanets (Boujibar et al., 2020; McDonough & Yoshizaki, 2021; Perryman, 2011; White, 2013). The discovery of some exoplanets orbiting their host star even closer than Mercury orbits the Sun (0.39 A.U.; Perryman, 2011), has drawn attention to the existence of exoplanets possibly having comparable sizes and internal structures to our rocky planets. The chemical composition of the nebula from which the solar system originated was highly heterogeneous, as reflected by chondritic compositions. Consequently, the planets in our solar system exhibit pronounced compositional zoning, correlated with the distribution of volatiles (also reflective of temperature variations in space and time), the oxygen fugacity (fO_2), which depends on the variation in the O_2/H_2 ratio between condensed matter (where O represents an important fraction) and nebular gas (dominated by H_2, the main reducing agent), and the metal/silicate ratio, as inferred from the varied compositions of chondrites (McDonough & Yoshizaki, 2021; Trønnes et al., 2019; White, 2013).

The solar system's four inner planets are strongly depleted in volatile elements relative to the Sun (White, 2013), suggesting that the inner regions of solar nebula were characterized by reduced chemistry, based on a different iron distribution with radial distance as driven by the magnetic field intensity in the protoplanetary disk (McDonough & Yoshizaki, 2021). The redox gradient in the protoplanetary nebula would result in planetary accretion close to the Sun likely producing Mercury-like objects (Cartier & Wood, 2019; Charlier & Namur, 2019), with low oxygen fugacity values. Our understanding of this chemical environment stems from the analysis of the physical and chemical properties of those materials believed to originate in a similar nebular environment. Reduced meteorites such as enstatite chondrites (EN), high-iron meteorites (CH), bencubbinites (CB), and aubrites serve as excellent candidates to describe the geochemistry of the innermost nebula (Cartier & Wood, 2019; Malavergne et al., 2010; Steenstra & van Westrenen, 2020), although CH and CB have been proposed by some authors (Kruijer et al., 2020; Warren, 2011) to be formed beyond Jupiter's orbit or from a different reservoir. Furthermore, reduced materials have also been considered among the precursor bodies that were then incorporated into Earth during accretion (e.g., Javoy et al., 2010; Wänke et al., 1984; Wohlers & Wood, 2015).

Here, we investigate how reduced materials such as enstatite chondrites, CH, and CB chondrites, and aubrites, affect the phase equilibria of exoplanets' interiors. In particular, we refer here to exoplanets whose maximum size is comparable to that of the Earth (1 M_E); which we will henceforth call sub-Earths, thus defining a category of exoplanets with dimensions comparable to those of Mercury and Mars. In addition, we call exo-Mercury, a subclass of exoplanets that are characterized by a radius, high core mass fraction, high density, Fe-enrichment, and, importantly, origin conditions dominated by low values of oxygen fugacity, comparable to Mercury. The term "super-Mercury" widely reported in literature (e.g., Unterborn et al., 2023) is referred exclusively to the high core mass fraction of these exoplanets, without defining neither the composition nor the birthplace chemical conditions. Therefore, a more specific definition of the term "exo-Mercury" which is straightforwardly related to those extrasolar planets, that share Mercury's size and properties, seems to be needed.

Mercury, accreted in the most reducing conditions reported for our solar system (Boujibar et al., 2019; Chabot et al., 2014; Knibbe & van Westrenen, 2015; Malavergne et al., 2014; McCubbin et al., 2012; Namur, Collinet, et al., 2016; Zolotov et al., 2013), is here employed as a proxy for elucidating the properties of exoplanets that exhibit analogous physical and chemical attributes. We model the mantle mineralogy of exoplanets formed in such reduced geochemical context and characterize the stability field of the phases as a function of the temperature and pressure conditions relevant for Mercury-size objects.

Section 2 details the adopted methodology, Section 3 describes the reduced materials assumed as precursors of exoplanets bulk silicate composition, and Section 4 presents the results of thermodynamic models. The estimated mineralogy for the mantle of these exoplanets is discussed in Section 5, while Section 6 addresses the implications on the thermochemical evolution of these exo-planets.

2. Methods

We model the mineral assemblages that would constitute a putative rocky mantle in the sub-Earths exoplanets at thermodynamic equilibrium as a function of temperatures (1200–1700 K) and pressures (3–5 GPa) by using the

Table 1
Bulk Silicate Compositions Used for Thermodynamic Calculations

Major oxides assumed as thermodynamic components

wt.%	Model #1	Model #2	Model # 3	Model # 4	Model # 5	Model # 6	Model # 7	Model # 8	Model # 9	Model #10
SiO_2	48.9	67.9	36.70	41.27	65.25	61.98	38	47.1	37.6	50.8
TiO_2	0.2	0.2	0.15	0.20	0.05	0.06	0.15	0.3	0.5	0.2
Al_2O_3	3.6	3.1	1.47	2.13	2.12	2.51	3.5	6.4	11.7	5.2
Cr_2O_3	0.8	1.1	0.4	0.53	0.09	0.10	0	3.3	0.2	0.7
FeO	4	0.3	1.34	4.01	0.42	0.50	0.5	3.7	3	2
MgO	38.8	25	19.43	26.08	26.92	31.70	32	33.7	36.1	37.4
CaO	2.6	0.1	1.19	2.21	1.43	1.70	3.5	5.2	10.7	3.6
Na_2O	0.4	0.01	0.61	1.31	1.02	1.20	0.2	0.08	0.1	0.04
K_2O	0.1	–	0.08	0.14	0.11	0.13	0	0	0	0.04
$(MgO + FeO)/SiO_2$	0.88	0.38	0.58	0.77	0.43	0.53	0.87	0.80	0.99	0.79

Note. Chemical analyzes of the major oxides, with percentages expressed by mass (wt. %) of CH chondrite-ALH85085 (Model# 1) (Anzures et al., 2020; Weisberg et al., 1988), CB ideal composition (Model# 2) (Brown & Elkins-Tanton, 2008; Malavergne et al., 2010), Bencubbin (Model #3) (II composition, Jarosewich, 1990), Cumberland Falls (Model #4) (Jarosewich, 1990) and Indarch (Model #5) (Berthet et al., 2009). Indarch SiO_2 depleted (Model #6) has been extrapolated by assuming that 20 wt. % of SiO_2 entered the core (after Nittler et al., 2018). The chemical analyzes of the major oxides, with percentages expressed by mass (wt. %) of additional bulk compositions, Composition 1 (Model #7) (Goettel, 1988), Composition 2 (Model #8) (Morgan & Anders, 1980), Composition 3 (Model #9) (Taylor & Scott, 2003), Composition 4 (Model #10) (Taylor & Scott, 2003) are indicated. $(MgO + FeO)/SiO_2$ ratios of each bulk composition is also reported.

software Perple_X (6.9.1 version) (Connolly, 1990). We assumed the temperature range suggested for Mercury's mantle by Rivoldini et al. (2009) and Rivoldini and Van Hoolst (2013). The minimum temperature (T) at the core-mantle boundary (CMB) has been suggested by Michel et al. (2013) and Tosi et al. (2013). The pressure (P) range is derived from Margot et al. (2018) and Steinbrügge et al. (2021). These values are within the T and P range of probable rocky-exoplanets modeled by Unterborn and Panero (2019).

We choose five different chondritic precursor materials to model the starting bulk silicate compositions for the rocky mantle of sub-Earth size exoplanets following the approach reported in previous literature (Charlier et al., 2013; Namur, Collinet, et al., 2016) also applied to icy moons (Cioria & Mitri, 2022; Grasset et al., 2000; Kuskov & Kronrod, 2005; Mueller & McKinnon, 1988; Néri et al., 2020). We adopted as precursor materials reduced meteorites, belonging to CB (Bencubbin chemical group), CH (Fe-rich carbonaceous chondrites), EN (enstatite chondrites), and aubrite (achondrites) (see Section 3). These materials are also characterized by different $(MgO + FeO)/SiO_2$ ratios (Table 1).

We point out that these materials reflect the expected chemical composition consisting entirely of reduced oxides that would characterize a mantle after core segregation. We performed our thermodynamic calculations at a fixed value of fO_2 ($\Delta IW = -5.4$), which represents an average of the values (-7 to -2.4) reported in the literature for Mercury mantle (Cartier & Wood, 2019; Malavergne et al., 2010, 2014; McCubbin et al., 2012; Namur, Collinet, et al., 2016; Zolotov et al., 2013). A value of -2.5 has been also suggested for the aubrite parent body (AuPB; Fogel, 2005; Steenstra & van Westrenen, 2020). However, we would point out that oxygen fugacity does not exert a significant influence on phase equilibria, due to the absence of multiple valence states (e.g., we assume that Fe is present only as Fe^{2+}) among the selected thermodynamic components, since, as mentioned above, we assumed entirely reduced oxides compositions as precursors.

For calculations, we employed the ds6.33 revision of the Holland and Powell (2011) thermodynamic database to describe the mantle mineralogy in the NKCFMASTCr (Na_2O-K_2O-CaO-FeO-MgO-Al_2O_3-SiO_2-TiO_2-Cr_2O_3-O_2) chemical system. In our models, we consider the following solution models (named HGP after Holland, Green, and Powell, 2018): orthopyroxene (Opx (HGP)), clinopyroxene (Cpx (HGP)), olivine (O (HGP)), spinel (Sp (HGP)), garnet (Gt (HGP)) (Holland et al., 2018), melt (melt (HGP)) (Heinrich & Connolly, 2022; Holland & Powell, 2003), and plagioclase (feldspar: Fuhrman & Lindsley, 1988). Supporting Information S1 provides further information about our modeling and methodology.

We focused our model on the simplified NKCFMASTCr system, initially neglecting other chemical components (e.g., sulfur, carbon). The results are presented through isochemical phase diagram sections, which show the stability field of the various mineral assemblages. Our free energy minimization calculations also yield the phase proportions, for all precursor materials modeled (Figure 6, see Tables S2 and S3 in Supporting Information S1) and the corresponding densities of the predicted phase assemblages (Table 2). As the mineral phases' equilibria were known, it was also possible to model the melting temperature for each model (Figure 10). In addition, using a Perple_X calculation option (see Table S1A in Supporting Information S1), the melt fraction produced in each phase assemblage, predicted to be stable, was also described in the same figure.

3. Reduced Materials in Inner Stellar Nebulae

In order to investigate a broad range of compositions ($0.62 <$ MgO + FeO/$SiO_2 < 1.8$) to constrain the mantle mineralogy of small exoplanets located in the inner region of their nebula, we considered their bulk silicate compositions to be a chondritic-like precursor material originated in low oxygen fugacity environments. We also evaluate some differentiated precursors, as aubrite group, suggested in the literature as possible Mercury's building blocks (Cartier et al., 2022; Udry et al., 2019). We also model a silica-depleted bulk silicate composition of Indarch, which has been extrapolated assuming that 20 wt. % of SiO_2 might entered the core, following Nittler et al. (2018). The different SiO_2 contents (Table 1) of precursor materials illustrate the effect of silica abundance on the balance between olivine and pyroxene in mantle mineralogy and on the core formation process.

3.1. Model 1: CH Precursor Material

The CH meteorites are polymict regolith breccias, distinguished by the high siderophile element content. The CHs have a high metal content (20 vol. %), consisting of kamacite α-(Fe, Ni), plessite (i.e., an intimate intergrowth of taenite and kamacite), and minor taenite γ-(Ni, Fe) and tetrataenite (FeNi) (Hutchison, 2004).

We choose to model the prototype ALH85085 (CH-3; e.g., a chondrite of the CH group with petrologic type 3) bulk composition, because it is abnormally metal-rich and sulfide-poor (0.25 wt.%; Wasson & Kallemeyn, 1990), with micron-sized metallic blebs (Scott, 1988), chondrules (C-cryptocrystalline, RP-radial pyroxene, BO-barred olivine textural types) and unaltered CAIs (i.e., calcium aluminum-rich inclusions). Weisberg et al. (1988) noted that some particles show reverse zoning (e.g., olivine core Fa-18, edge Fa-12), indicating reduction. Moreover, CH group is closely related to CB group chondrite (Clayton & Mayeda, 1999; Grady & Pillinger, 1990; Ivanova et al., 2006). This bulk silicate composition has already been reported in the literature as Mercury's mantle analog (Anzures et al., 2020).

3.2. Model 2: CB (Ideal Composition) Precursor Material and Model 3: Bencubbin Precursor Material

CB chondrites are unique polymict breccias containing abundant metal (almost 60 wt. % for CBa sub-group members, like Bencubbin; Weisberg et al., 1998) and highly reduced silicates ($Fs_{<3}$, $Fa_{<3}$, Weisberg et al., 1998). These properties led researchers to conclude that CBs originated at $\Delta IW = -2.5$ and -5.5, in agreement with fO_2 values suggested for Mercury (Malavergne et al., 2010) and probably resembling fO_2 conditions in other inner stellar nebulae.

We modeled both a CB ideal bulk silicate composition (Model 2) and Bencubbin II bulk silicate composition (Model 3).

CB ideal bulk silicate composition is our benchmark, since it was studied by Malavergne et al. (2010) (derived from data contained in Brown and Elkins-Tanton (2008) and Schoenbeck and Palme (2003, 2005)), who modeled the phase equilibria in a putative Mercury silicate mantle by using MELTS software. Brown and Elkins-Tanton (2008) proposed the use of a CB averaged bulk composition as precursor material to model the solidification of Mercury's magma ocean, since these chondrites were characterized by an unusually high metallic content. In previous literature (Brown & Elkins-Tanton, 2008; Taylor & Scott, 2001; Weisberg et al., 2001), it was argued that accretion of metal-rich CB chondritic planetesimals could be a plausible alternative to previous models of Mercury's origin (Benz et al., 1988; Cameron, 1985; Fegley & Cameron, 1987). Bencubbin II bulk silicate composition was extrapolated by Jarosewich (1990) (see also Table 1).

Table 2
Density Values Modeled for Each Bulk Compositions Assumed as Precursor Material

Precursor material	Density (kg m^{-3}) at 1200 K- 3 GPa	Density (kg m^{-3}) at 1700 K- 5 GPa
ALH85085	3256.2	3261.4
CB id.comp.	3077.9	3190.8
Bencubbin	3197.3	3230.4
Cumberland Falls	3235.2	3236.3
Indarch	3114.9	3185.5
Indarch SiO$_2$ depleted	3183.6	3217.1

3.3. Model 4: Aubrite-Like Composition Precursor Material

Aubrites are reduced samples believed to have originated from a partially, if not fully, differentiated and highly reduced parent body (Casanova et al., 1993; Keil, 2010; Lodders et al., 1993; Steenstra, Seegers, et al., 2020, Steenstra, Trautner, et al., 2020), composed largely of FeO-free enstatite. Cumberland Falls is a polymict breccia, so defined because hosts OC clast and OC-impact melt breccias containing shocked OC material (Rubin & Ma, 2021). We decided to investigate also this composition to verify whether the mineral assemblage matches the mineralogy derived from enstatite-chondrite, since aubrites have been proposed as resulting from the partial melting of EN chondrites.

Furthermore, aubrite parent body has probably been formed under low fO$_2$ (ΔIW = −4.4; Casanova et al., 1993; Wadhwa, 2008), and aubrite achondrites have also been proposed as Mercury building blocks material (Burbine et al., 2002; Cartier et al., 2022; Steenstra, Trautner, et al., 2020; Udry et al., 2019; Wilbur et al., 2022).

3.4. Model 5: EN Precursor Material

The enstatite chondrites are commonly subdivided into 2 sub-groups according to their amount of metallic iron: EH (Fe-rich enstatite chondrites) and EL (Fe-poor enstatite chondrites) (Kallemeyn & Wasson, 1986; Keil, 1968; Sears, 1980). Enstatite chondrites are the most reduced meteorites (Barrat et al., 2014; Brett & Keil, 1986; Defouilloy et al., 2016; Keil, 1968; Mason, 1966; Rubin, 1984; Weisberg & Kimura, 2012). These meteorites are thought to be formed at ΔIW = −4 and −5.5, compatible with fO$_2$ values suggested for Mercury (Malavergne et al., 2010). Besides, they are believed to be a suitable analog for the Mercurian mantle (Nittler et al., 2018, also in depleted SiO$_2$ abundance; Cartier & Wood, 2019; Steenstra & van Westrenen, 2020). Moreover, Indarch has also been employed to address planetary differentiation processes in reduced environments (Berthet et al., 2009; McCoy et al., 1999).

Therefore, we decided to also include the bulk silicate composition of Indarch (EH-4; e.g., enstatite chondrite of the EH group with petrologic type 4) in our modeling.

4. Results

We present the results of the modeled mineral assemblages forming the possible reduced mantles of sub-Earth exoplanets. The chemical composition of predicted stable phases is reported in Tables S2 and S3 of Supporting Information S1.

4.1. Model 1: CH Precursor Material

This mineral assemblage for Model 1 assumes a CH chondrite as precursor material. The phase diagram section derived from Allan Hills 85085 reveals that olivine, clinopyroxene, orthopyroxene, and garnet are the stable mineralogy as a function of pressure (P) and temperature (T) in all runs, except the 3 GPa- 1700 K run, where the predicted stable mineral assemblage is given by opx + ol + cpx. Figure 7 and Tables S2 and S3 in Supporting Information S1 present the phase proportions mass amount (wt.%) of each phase for two different P-T conditions, 1200 K- 3 GPa, and 1700 K- 5 GPa, respectively. In more detail, orthopyroxene, that is, a series between enstatite (Mg$_2$Si$_2$O$_6$) and ferrosilite (Fe$_2$Si$_2$O$_2$) end-members, is stable in each field defined in the diagram, forming up to 46 wt.% of the rock (Figure 6; Tables S2 and S3 in Supporting Information S1). Orthopyroxene has an average
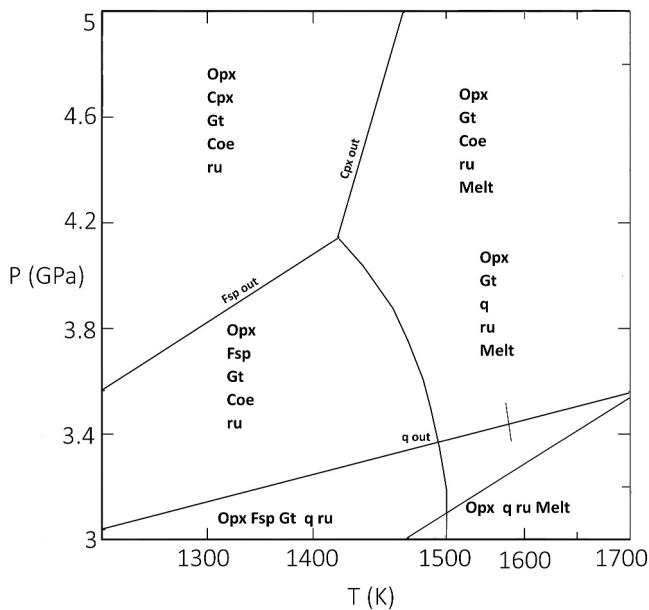
Figure 1. Model 2: Isochemical phase diagram section derived from CB ideal bulk silicate composition, showing the stability field of the minerals as a function of the pressure (*P*) and the temperature (*T*). *Ol* (olivine); *Cpx* (clinopyroxene); *Fsp* (feldspar); *Gt* (garnet); *Opx* (orthopyroxene); *q* (quartz); *ru* (rutile); *Coe* (coesite); *Melt* (melt).

density of 3,300 kg m^{-3} and is rich in the enstatite component (En$_{90}$). Olivine and clinopyroxene are also stable in every field, forming ~30 and ~10 wt.%, respectively. Olivine is mostly forsteritic in composition, while clinopyroxene is mostly diopsidic (CaMgSi$_2$O$_6$), with minor amounts of jadeite (NaAlSi$_2$O$_6$). Both minerals have an estimated density of 3,200 kg m^{-3}. The garnet-group minerals occur as minor phases.

4.2. Model 2: CB (Ideal Composition) Precursor Material

Model 2 mineralogy is dominated by orthopyroxene and accessory phases, such as garnets and SiO$_2$ polymorphs (Figure 1). Clinopyroxene is indicated in the isochemical phase diagram section, but it is present in a very negligible amount (0.06 wt.%).

Orthopyroxene is stable in every field defined in the diagram, forming ~60 wt.% (Figure 6; Tables S2 and S3 in Supporting Information S1). This phase has an average density of 3,200 kg m^{-3} and is almost pure enstatite, with a minor amount of Ti and Al. The garnet-group minerals occur as minor phases. Pyrope (i.e., Mg-rich garnet, Mg$_3$Al$_2$(SiO$_4$)$_3$) is the most abundant, having an estimated density of 3,500 kg m^{-3}. Garnet forms ~10 wt.% of the assemblage. Finally, silica-polymorphs also represent important phases: quartz (beta-quartz) occurs at the lowest temperatures and pressures, forming ~30 wt.% of the assemblage, while coesite results to be stable at higher ones (see Figure 6; Tables S2 and S3 in Supporting Information S1). Finally, at low temperature and pressure, K-feldspar is present in a minor amount (0.06 wt. %) and has a sanidine (K(AlSi$_3$O$_8$)) composition. Rutile is present as a minor phase.

4.3. Model 3: Bencubbin Precursor Material

Model 3 mineralogy is dominated by orthopyroxene and accessory phases, such as garnets, quartz (at lower pressure), and coesite (at higher pressure) (Figure 2).
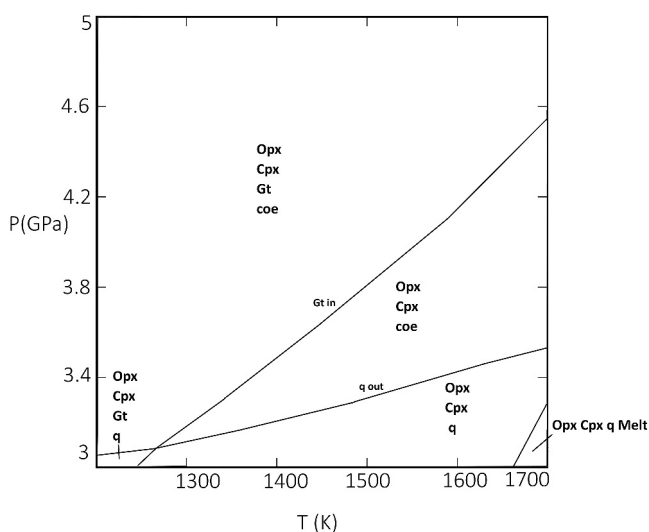
Orthopyroxene is stable in every field defined in the diagram, forming almost the 80 wt.% (Figure 6; Tables S2 and S3 in Supporting Information S1). This phase has an average density of 3,200 kg m^{-3}. The garnet-group minerals occur as minor phases. Garnet forms ~13 wt.% of the assemblage. Finally, silica-polymorphs also represent important phases: quartz (beta-quartz) occurs at low temperatures and pressures, forming ~7 wt.% of the assemblage, while coesite results to be stable at higher ones (see Figure 6; Tables S2 and S3 in Supporting Information S1).

Model 2 and Model 3 mineral assemblages are quite similar; however, Model 2 is more silica rich, containing significative abundances of quartz and feldspar at lower pressures and coesite at higher pressures. Model 3 contains significant cpx, while Model 2 is garnet richer. Some Ca goes also in feldspar stable in Model 2. Moreover, the feldspar represents the major store location for potassium, while in Model 3, all potassium is stored in clinopyroxene (see also Tables S2 and S3 in Supporting Information S1).

4.4. Model 4: Aubrite-Like Composition Precursor Material

This mineral assemblage derived for Model 4 is obtained by assuming aubrite achondrite as precursor material. Figure 3 presents the pseudo section derived from Cumberland Falls and shows the *P-T* stability field of the mineral phases. Figure 6 and Tables S2 and S3 in Supporting Information S1 present the phase proportions mass amount (wt.%) of each phase for two different PT conditions of 1200 K- 3 GPa, and 1700 K- 5 GPa, respectively. The predicted

Figure 2. Model 3: Isochemical phase diagram section derived from Bencubbin II (Jarosewich, 1990; CB chondrite) bulk silicate composition, showing the stability field of the minerals as a function of the pressure (*P*) and the temperature (*T*). *Cpx* (clinopyroxene); *Gt* (garnet); *Opx* (orthopyroxene); *q* (quartz); *coe* (coesite); *Melt* (melt).

assemblages for Model 4 are dominated by ferromagnesian silicates, which can be distinguished between three main groups: olivine, orthopyroxene, and clinopyroxene (Figure 3). Orthopyroxene is stable in every field defined in the diagram, forming an average of ~45 wt.% (Tables S2 and S3 in Supporting Information S1). Orthopyroxene has an average density of ~3,200 kg m^{-3} and is almost pure enstatite. Olivine is also stable in every field, forming ~16 wt.%. Olivine is almost pure forsterite in composition and has an estimated density of ~3,200 kg m^{-3}. Clinopyroxene is the most abundant phase after orthopyroxene at the lowest temperature and the most abundant phase of the entire assemblage at the highest ones (Figure 6, Tables S2 and S3 in Supporting Information S1). Its composition is mainly jadeitic. Garnet occurs in a negligible wt.% (0.58 wt.% at high *P-T*). The decrease in the modal abundance of clinopyroxene with increasing pressure is related to the presence of garnet as the Ca-bearing phase.

4.5. Model 5: EN Precursor Material

This mineral assemblage derived for Model 5 is obtained assuming EN chondrite as precursor material. Figure 5 presents the isochemical section derived from Indarch and shows the stability field of the minerals as a function *P* and temperature *T*. Figure 6 and Tables S2 and S3 in Supporting Information S1 present the phase proportions mass amount (wt.%) of each phase for two different cases with fixed temperature and pressure of 1200 K and 3 GPa, and 1700 K and 5 GPa, respectively. The predicted assemblages for Model 5 are dominated by pyroxene minerals. Orthopyroxene, is stable in every field defined in the diagram, forming ~60 wt.% (Figure 6, Tables S2 and S3 in Supporting Information S1). This phase has an average density of 3,300 kg m^{-3} and is almost pure enstatite in composition. Clinopyroxene is mostly diopsidic ($CaMgSi_2O_6$) and jadeitic ($Na(Al,Fe^{3+})Si_2O_6$) in composition. It represents ~15 wt.% and has an estimated density of 3,200 kg m^{-3}. Similarly, to Model 2 mineralogy, SiO_2 polymorphs show significative abundance up to ~20 wt.% (Figure 6, Tables S2 and S3 in Supporting Information S1).

Model 5 is richer in quartz than Model 6, and richer in clinopyroxene than Model 2.

4.5.1. Model 6: EN With a Depleted SiO_2 Content

This mineral assemblage derived for Model 6 is obtained assuming an EN-silica depleted chondrite as precursor material. Figure 6 presents the pseudo section derived from Indarch and shows the stability field of the minerals as a function of *P-T*. Figure 6 and Tables S2 and S3 in Supporting Information S1 present mass amount (wt.%) of each phase for two different *P-T* conditions of 1200 K and 3 GPa, and 1700 K and 5 GPa, respectively. The predicted assemblages for Model 6 are dominated by pyroxene minerals. Orthopyroxene is stable in every field defined in the diagram, forming >60 wt.% (Figure 6, Tables S2 and S3 in Supporting Information S1). This phase has an average density of 3,300 kg m^{-3} and is almost pure enstatite in composition. Clinopyroxene is mostly diopsidic ($CaMgSi_2O_6$) and jadeitic ($Na(Al,Fe^{3+})Si_2O_6$) in composition. It represents ~20 wt.% and has an estimated density of 3,200 kg m^{-3}. Unlikely the non-depleted Model 2 and Model 5 mineral assemblages, SiO_2 polymorphs do not show significative abundance (<10 wt.%, Figure 6, Tables S2 and S3 in Supporting Information S1). This lower abundance is undoubtedly associated with the reduced quantity of SiO_2 assumed in the initial bulk composition.

Model 5 and Model 6 mineral assemblages are very similar, but the predicted stable phase named "melt" appears at slightly different temperatures (see Figures 4 and 5). Model 6, based on a less silica-rich bulk composition, presents a melt stable at lower temperatures than Model 5.

4.6. Density of the Modeled Mineral Assemblages and Related Mantle Density

The calculated mantle densities range for all Models between 3,100 and 3,300 kg m^{-3} (Table 3). These results will be discussed in Section 5.

5. Discussions

In this section, we discuss the results obtained from our modeling and present a comparison between our findings and results from previous literature.
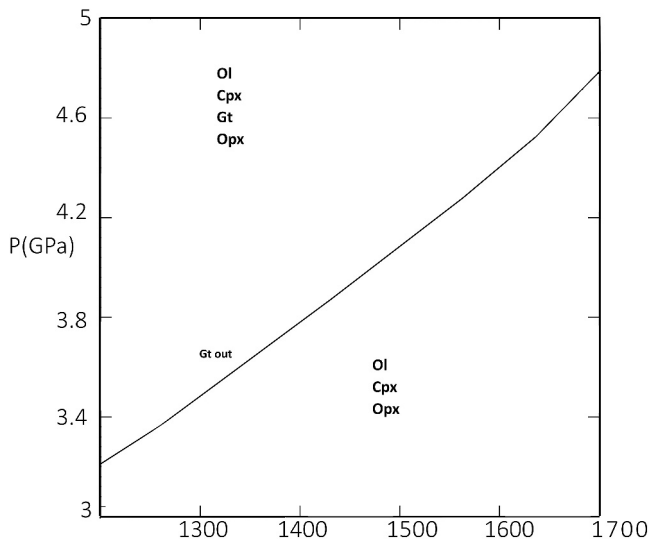
Figure 3. Model 4: Isochemical phase diagram section derived from Cumberland Falls (aubrite) bulk silicate composition, showing the stability field of the minerals as a function of the pressure (*P*) and the temperature (*T*). *Ol* (olivine); *Cpx* (clinopyroxene)*; Gt* (garnet)*; Opx* (orthopyroxene).

5.1. Mineralogical Composition of Sub-Earths and Exo-Mercuries

The mineralogy of these categories of exoplanets is poorly constrained, unlike super-Earth-sized objects (Boujibar et al., 2020; Perryman, 2011; White, 2013). Planetary environments dominated by reducing conditions have been underexplored, although Mercury and significant groups of meteorites (e.g., enstatite chondrites) exhibit clear evidence of having formed under such conditions. Therefore, the mineral assemblages that would constitute the mantles of sub-Earth-sized exoplanets in the inner regions of other stellar systems are largely uncertain. Previous works attempted to decipher the mantle composition of exoplanets through the abundances of planet-building elements (e.g., Si, Al, Mg, Fe, Ca) estimated for their parental star (Hinkel & Unterborn, 2018; Putirka & Rarick, 2019; Putirka & Xu, 2021). Hinkel and Unterborn (2018) described the planetary mineralogy of Earth-sized exoplanets starting from the stellar compositions reported in Hypatia Catalog (Hinkel et al., 2014, 2016) by using ExoPlex, a thermodynamically self-consistent mass-radius-composition calculator. ExoPlex is largely employed in constraining the mineralogy of extrasolar planets (Hinkel & Unterborn, 2018; Unterborn et al., 2023). However, this calculator takes into account major components (i.e., Si, Al, Mg, Ca, Fe, O), neglecting minor ones (i.e., Ti, Cr, Na, and K), that are considered in our model.

Similarly, Putirka and Rarick (2019) and Putirka and Xu (2021) tried to obtain a normative mineralogy of exoplanets mantles starting from the stellar abundances described in the same stellar catalog. They followed an algebraic methodology (Thompson, 1982) to recast oxide compositions into mineral proportions, after having chosen adequate mineral compositions. It is important to note that these models rely on the compositional connection between parental star and its planetary system.

We outlined several models describing mineral assemblages stable at sub-Earth (e.g., Mercury-sized) pressures, temperatures, and low-oxygen fugacity conditions (see Section 4), using Mercury as analog. Our models also rely on the assumption that the nebulae of the exoplanets here considered have physical and chemical properties similar to the solar nebula, with composition of parental stars comparable to that of the Sun.
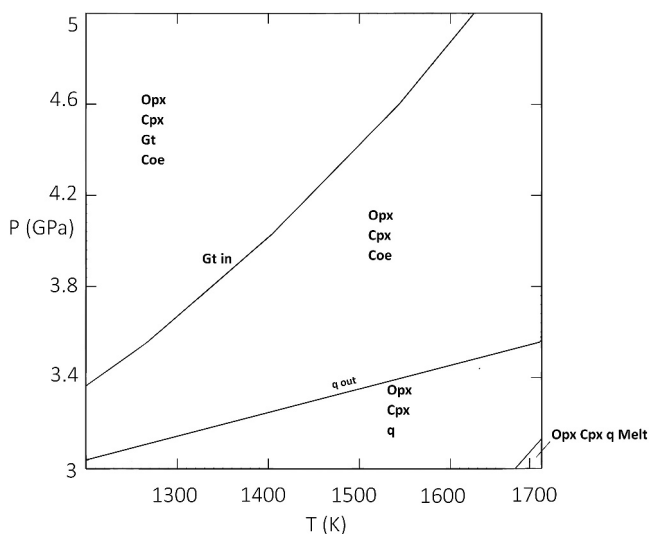

Figure 4. Model 5: Isochemical phase diagram section derived from Indarch (enstatite chondrite) bulk silicate composition, showing the stability field of the minerals as a function of the pressure (*P*) and the temperature (*T*). *Cpx* (clinopyroxene)*; Gt* (garnet)*; Opx* (orthopyroxene)*; q* (quartz); *coe* (coesite); *Melt* (melt).

Our thermodynamic simulations revealed that mantles formed under reducing conditions, as expected for the inner regions of stellar nebulae, may be pyroxene-dominated. These mineral assemblages are quite different from the Earth's mantle mineralogy, where olivine is the main mineral constituent peridotite rocks (Best, 2013; Philpotts & Ague, 2022). Venus and Mars are also believed to have a mantle mineralogy similar to that of Earth. The Martian mantle is thought to be primarily composed of olivine, along with its high-pressure phases, which increase in abundance with depth (Yoshizaki & McDonough, 2020). An useful insight into the mineralogy of Mars comes from meteorites (SNCs), which sample Martian mafic and ultramafic rocks (Hutchison, 2004; Rubin & Ma, 2021). Mineral assemblages in the upper mantle of Venus are expected to be quite analogous to those found in the terrestrial mantle, as Venus has experienced a similar range of pressure and temperature conditions (Smrekar et al., 2007). Given that Mercury is thought to have originated in a similar geochemical environment and considering the boundary conditions assumed for this modeling (e.g., precursor materials adopted, *P-T* ranges), we propose that Mercury's mantle is also richer in pyroxene than the other terrestrial planets.

A main conclusion of our models is that pyroxenes are the most abundant phases in each model composition (see Section 4). This outcome agrees with the findings shown in Putirka and Rarick (2019) where the lower (Mg + Fe)/Si ratio in the mantle results in a greater amount of pyroxene. We explored the correlation between (Mg + Fe)/Si ratio and SiO_2 abundances in precursor
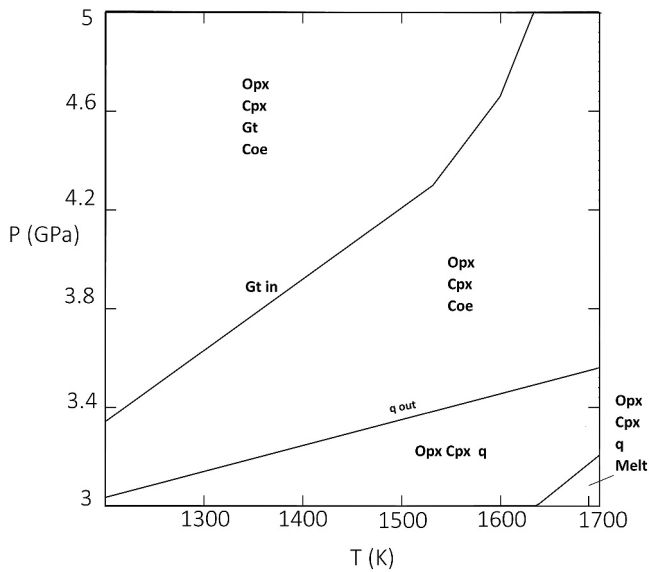
Figure 5. Model 6: Isochemical phase diagram section derived from Indarch (enstatite chondrite)-depleted bulk composition, showing the stability field of the minerals as a function of the pressure (*P*) and the temperature (*T*). *Cpx* (clinopyroxene)*; Gt* (garnet)*; Opx* (orthopyroxene); *q* (quartz); *coe* (coesite); *Melt* (melt materials).

materials and the resulting mineral assemblages at equilibrium (Figures 7 and 8). Figure 7 shows the mineral composition for each model at 3 GPa- 1200 K in a ternary clinopyroxene-olivine-quartz diagram. This illustrates the relationship between silica content in the assumed precursor materials and the resulting ferromagnesian phases' abundances in the predicted mineral assemblage. The mineral assemblages containing olivine are quartz-free, while the olivine-depleted assemblages present variable amounts of quartz. For example, the orange dot in Figure 7 indicates that the mantle- derived from an enstatite precursor material (Model 5) is formed by quartz and clinopyroxene, with no olivine.

This is a direct consequence of the relationship between silica abundance in the assumed precursor materials and olivine/orthopyroxene stability fields, determined by the reaction Mg_2SiO_4 (forsterite) $+$ $SiO_2 = Mg_2Si_2O_6$ (enstatite).

To further explore the silica content effect on resulting mineralogy, we modeled additional bulk compositions besides the ones already reported in the results section. This was done to account for a range of SiO_2 contents, ranging from 37.3 wt. % (Composition 3, Taylor & Scott, 2003) to 67.9 wt. % (Model 2, Malavergne et al., 2010). Specifically, equilibrium mineral assemblages were calculated for compositions suggested by Malavergne et al. (2010) and Nittler et al. (2018), as suitable analogs for Mercury: Composition 1 was derived from Goettel (1988); Composition 2 from Morgan and Anders (1980); Composition 3 from Taylor and Scott (2003). Composition 4

represents a variant of the latter but with the addition of metals (Taylor & Scott, 2003). For a more detailed description of these bulk silicate compositions, please refer to the references mentioned therein. The methodology, the values of *P* (3–5 GPa) and *T* (1200–1700 K), and the thermodynamic boundary conditions are the same as described in Section 2 for models 1, 2, 3, 4, and 5.

These additional results emphasize that the balance between pyroxene and olivine is related to SiO_2 abundance of the system (Ebel & Stewart, 2018). However, in low-oxygen fugacity environments, it is important to consider that Si could exhibit a siderophile behavior (Cartier & Wood, 2019; Cartier et al., 2020; Kilburn & Wood, 1997; Steenstra, Trautner, et al., 2020), potentially forming alloys with iron from the core (Edmund et al., 2022; Lark et al., 2022; Righter et al., 2020; Yokoo et al., 2023). Therefore, the amount of SiO_2 available in the mantle is closely linked to evolution of the core, which itself depends on the chemical conditions during the planetary body differentiation. Additionally, the incorporation of Si into the core is influenced by the presence of other light elements that can potentially bind to iron (Dasgupta et al., 2009; Kilburn & Wood, 1997; Rohrbach et al., 2007). This confirms that core size and composition have a first-order constraint on the mantle mineralogy, as previously noted (Putirka & Rarick, 2019). Recently, it has been highlighted how the presence of S and C as light elements in the iron alloy of Mercury's core could restrict the Si content within the core (Edmund et al., 2022; Lark et al., 2022). An increased silica amount incorporated in the core would result in an olivine-rich mantle composition. Hence, it becomes clear that the mantle's mineralogy could have significant implications for the

Table 3
Exo-Mercuries Mantle Compositions Deduced From Our Mineral Assemblage (After Putirka and Rarick (2019))

Composition (wt.%)	Standard mineralogy (Putirka & Rarick, 2019)	Models
$\frac{MgO+FeOt}{SiO2} < 0.62$	Quartz-normative pyroxenite	2 3 5 6
$0.62 < \frac{MgO+FeOt}{SiO2} < 0.85$	Pyroxenite	4 C2 C4
$0.85 < \frac{MgO+FeOt}{SiO2} < 1.8$	Peridotite	1 C1 C3
$\frac{MgO+FeOt}{SiO2} > 1.8$	Magnesiowüstite normative Peridotite	–

Note. Models reported as C1, C2, C3, and C4 are referred to the additional models given by Composition 1 (Goettel, 1988), Composition 2 (Morgan & Anders, 1980), Composition 3 (Taylor & Scott, 2003), Composition 4 (Taylor & Scott, 2003).
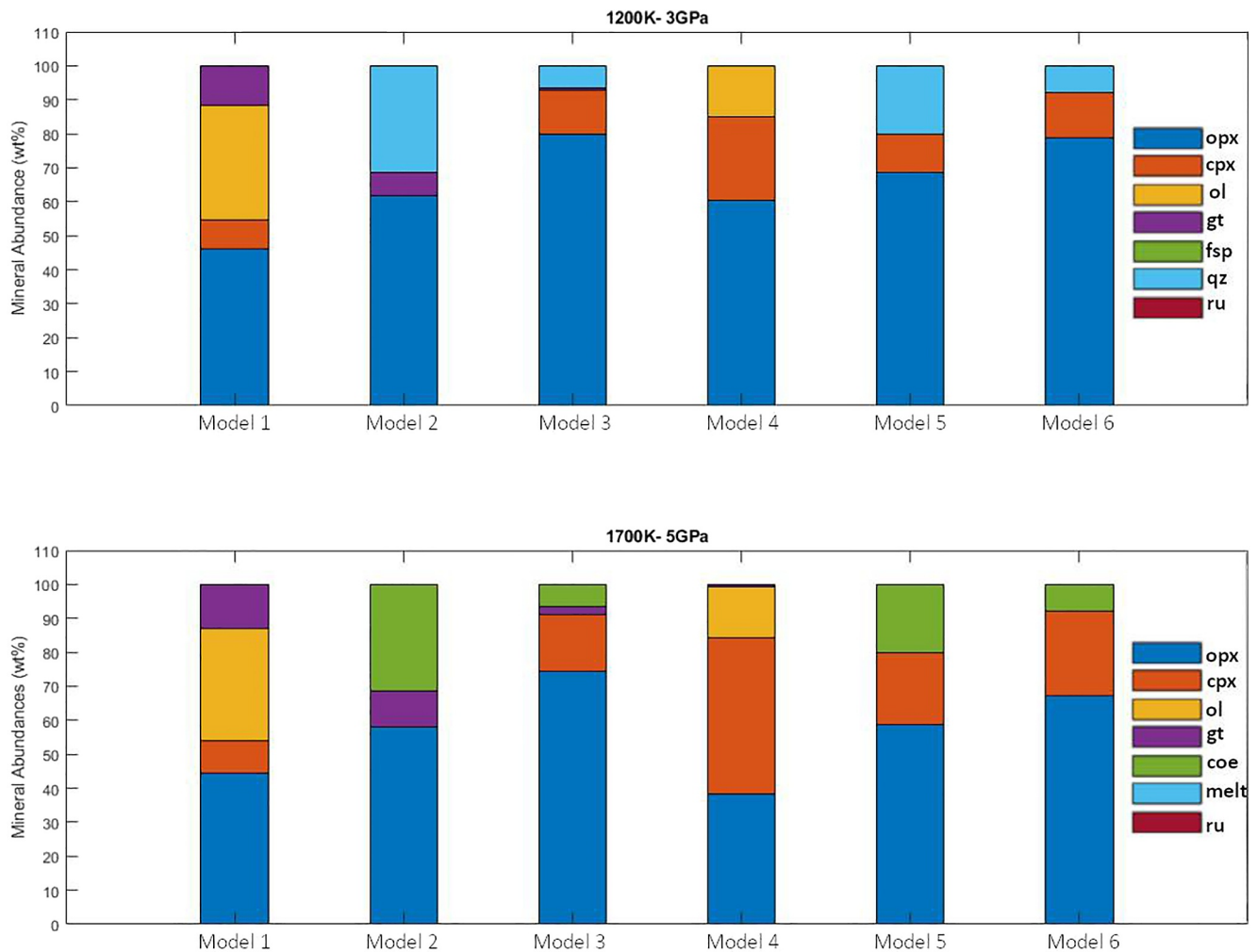
Figure 6. Bar graphs showing the mineral abundances for each Model at 1200 K- 3 GPa (upper panel) and at 1700 K- 5 GPa (bottom panel). The modeled bulk silicate compositions are *CH* (Model 1); *CB ideal* (Model 2); *Bencubbin* (Model 3); *aub* (Model 4); *EN* (Model 5); *EN dep.* (Model 6). Mineral phases are reported in legend. Rutile, melt, and feldspar are present in minimum amount and do not compare in the bar. Their abundances are indicated in Tables S2 and S3 of Supporting Information S1.

entire system of a sub-Earth, if complete differentiation occurred, since the elements' partitioning, which depends on their geochemical behavior, could affect both mantle and core compositions.

We also consider the (MgO + FeO)/SiO_2 ratios for each model and additional bulk compositions (see Figure 8). In general, since enstatite and forsterite possess the same Mg-proportion (2 mol of Mg), their equilibrium should not be influenced by the abundance of Mg, which is relatively high for all models shown here (>18 wt.%). However, upon analyzing the (MgO + FeO)/SiO_2 ratio, it is observed that a higher ratio results in a larger abundance of olivine. Figure 8 shows that compositions having a higher value of (MgO + FeO)/SiO_2 ratio tend to be olivine-rich, while the ones with lowest values result in olivine-free mineral assemblages.

Putirka and Rarick (2019) offered a useful classification of rocks in exoplanetary mantles, based on the Fe + Mg/Si ratio. Based on the Fe + Mg/Si ratio, it is possible to classify the resulting mineral assemblages as quartz-normative pyroxenite, pyroxenite, and peridotite. Following this scheme, we can define our resulting mineral assemblages as illustrated in Table 3.

According to the classification above, we can distinguish between two main mantle rock assemblages: pyroxenites (olivine-free mantle mantles) and peridotites (olivine-bearing mantles).
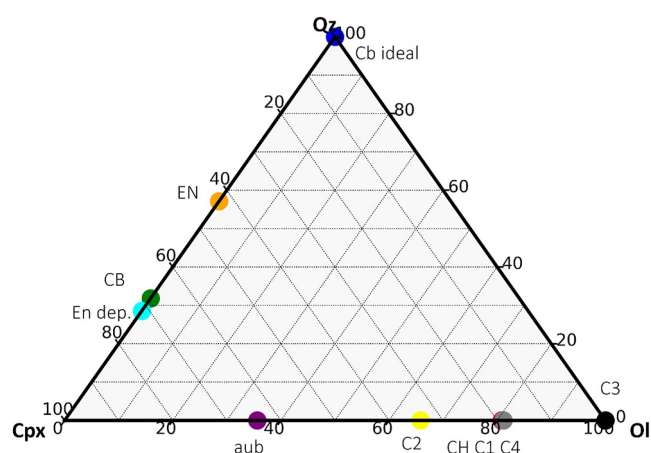
Figure 7. Ternary diagram showing the mineral abundances of each model as Ol, Cpx and Qz (wt.%) proportions. The modeled bulk compositions are *CH* (Model 1); *CB ideal* (Model 2); *CB* (Model 3); *au* (Model 4); *EN* (Model 5); *EN dep.* (Model 5, SiO$_2$ depleted). The additional models are C1(Model 7, Goettel, 1988; Nittler et al., 2018); C2 (Model 8, Morgan & Anders, 1980; Nittler et al., 2018); C3 (Model 9, Nittler et al., 2018; Taylor & Scott, 2003); C4 (Model 10, it is equal to Composition 3 plus metals; Nittler et al., 2018; Taylor & Scott, 2003).

5.2. Olivine-Bearing Mantles

Model 1 and Model 4 mineral assemblages present 40 and 15 wt.% of olivine respectively. The abundances of orthopyroxene are 45 wt.% and 65 wt.% respectively, while the clinopyroxene abundances are 10 and 25 wt.% respectively (Figure 6, 1200 K- 1 GPa). Both models do not contain quartz.

Model 1 (CH bulk composition), and additional composition modeled C1 and C3, could be considered to have a peridotite-like composition since these are all characterized by SiO$_2$ amounts <50 wt.% and MgO >30 wt.%. The resulting mineral assemblages predicted include olivine, orthopyroxene, clinopyroxene, and minor garnet. We can compare Model 1 (CH) stable phases with KLB-1 model for terrestrial peridotite. We refer here to the model presented by Holland et al. (2018). This model represents a refinement of the investigation offered by Jennings and Holland (2015) (see Figures S2 and S3 in Supporting Information S1). The predicted mineral assemblage of ol + cpx + opx + gt dominates the entire P-T field in model 1, except at 3 GPa and 1700 K, where gt disappears. This field is completely included in the gt + cpx + opx + ol stability field shown in P–T pseudo section calculated for KLB-1 in the KNCFMASTOCr system by Holland et al. (2018) (Figure 3 of this paper). Some discrepancies should be noted in garnet and orthopyroxene stability fields. Indeed, gt disappears in our modeling at 1700 K- 3 GPa, while it is stable at higher *T* in the KLB-1. Conversely, orthopyroxene destabilized at 3 GPa- 1680 K in KLB-1, but in Model 1 Opx is always stable. The expansion of the garnet-stability field in Holland et al. (2018) may derive from metastable phases computed in THERMOCALC code used to calculate KLB-1 pseudo section. For further information, refer to Holland et al. (2018). In any case, there is a general agreement between the phase boundary illustrated in Figure 1 and KLB-1.

Model 4 (aubrite bulk composition) shows the same mineral assemblage of Model 1, but the amount of olivine is lower (i.e., 15 wt.%) and could be considered a pyroxenite, if the same scheme is followed. Model 4, Composition 2 and 4 are all characterized by SiO$_2$ amounts ranging from 41 wt.% to 50 wt.% and MgO ranging from 27 wt.% to 40 wt.%. Model 1 and Model 4 mineral assemblages are quite similar, except for the garnet stability field. While Model 4 has garnet stable at the highest pressure, Model 1 shows this phase stable at any pressure and temperature, except at 1700 K and 3 GPa. This discrepancy could be attributed to different abundances in clinopyroxene and garnet (see also Tables S2 and S3 in Supporting Information S1). Model 4 shows a greater abundance of clinopyroxene, and we can therefore infer that Cpx is the main phase where calcium is stored at low *P* and *T*, while in Model 1 calcium is distributed between garnet and clinopyroxene at any *P* and *T* (except at 1700 K- 3 GPa).

In addition, the aubrite-precursor material results in the clinopyroxene-most rich mantle mineralogy among all other materials (see Figure 6). Therefore, it would be better classified as clinopyroxenite (olivine-websterite), having an average amount of olivine of 15 wt.%, orthopyroxene of ∼45 wt.% and clinopyroxene >30 wt.%.

The evolution of these mantles could be different from orthopyroxene richer mantles. As shown by Figure 10, orthopyroxene and clinopyroxene possess a similar viscosity. Moreover, in a geochemical reduced environment, this mantle could be richer in sulfide than others, since the anion S^{2-} tends to bound with cations (e.g., Ca^{2+}, Mg^{2+}) destabilizing silicates, as clinopyroxenes (i.e., diopside).

The predicted mineral assemblages of Composition 1, Composition 2, Composition 3, and Composition 4 are all olivine-bearing, showing variable amounts of forsterite (see Figure S2 in Supporting Information S1). Composition 3, which is the least silica-rich among all the investigated bulk compositions, is olivine dominated, with minor amounts of spinel, at lower pressures and temperatures; while at higher pressures, garnet is the second most abundant phase. Minor melt becomes also stable. While olivine is present in Composition 1, Composition 2, and Composition 4, enstatite is most abundant. Considering Putirka and Rarick (2019) classification scheme, these assemblages can be assumed to be peridotite-like (C1, C3) and pyroxenite-like (C3, C4) (see Table 3). Peridotite-
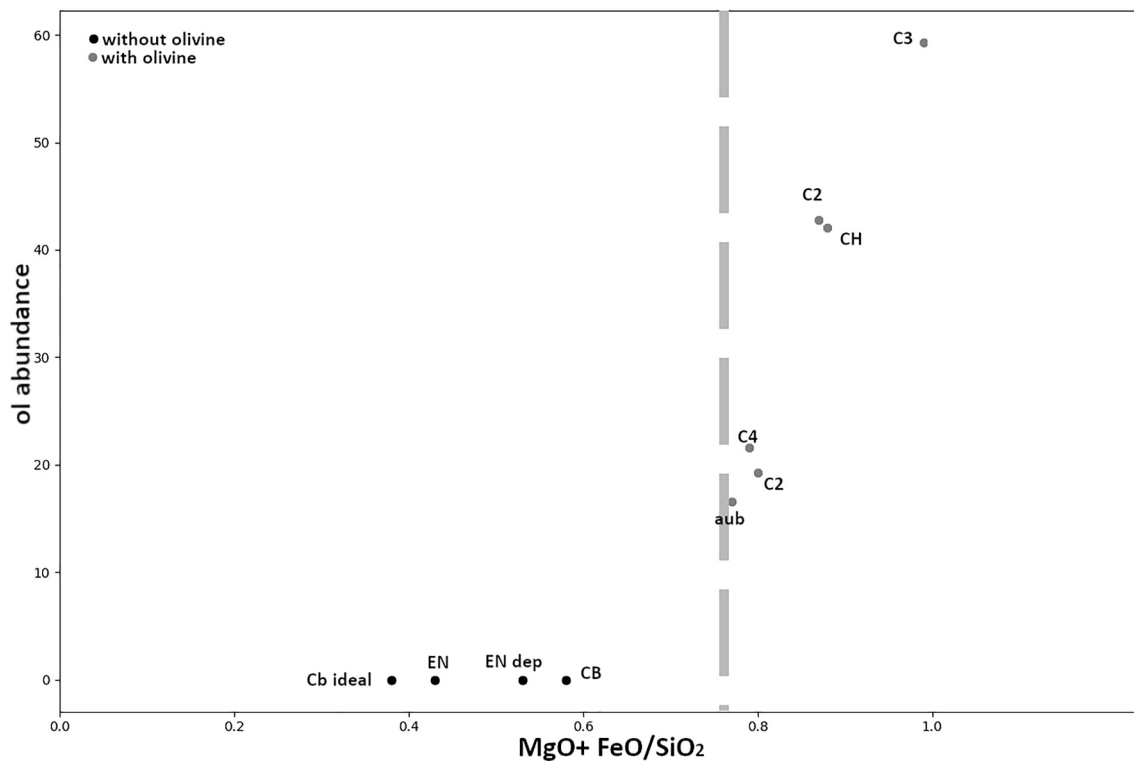
Figure 8. Correlation between olivine abundance and the MgO + FeO/SiO$_2$ ratio shown in precursor materials. The values reported are extrapolated at 1200 K- 3 GPa for each model. The modeled bulk compositions are *CH* (Model 1); *CB ideal* (Model 2); *CB* (Model 3); *aub* (Model 4); *EN* (Model 5); *EN dep.* (Model 6). The additional models are: *C*1 (Model 7, Goettel, 1988; Nittler et al., 2018), *C*2 (Model 8, Morgan & Anders, 1980; Nittler et al., 2018), *C*3 (Model 9, Taylor & Scott, 2003; Nittler et al., 2018), *C*4 (Model 10, it is equal to Composition 3 plus metals; Taylor & Scott, 2003; Nittler et al., 2018). The dashed, gray line separates olivine-free mineralogy from olivine-bearing mineralogy.

like associations are richer in clinopyroxene than pyroxenite-like associations, which show garnet over-stabilized with respect to clinopyroxene at low *P-T*.

5.3. Olivine-Free Mantles

Models 2, 3, 5, and 6 do not present olivine in resulting stable mineral assemblages. Enstatite is the dominant phase, followed by variable amounts of clinopyroxene and quartz. All models can be classified as quartz-bearing pyroxenites according to Putirka and Rarick (2019).

Model 2 and Model 3 are both based on CB-like bulk composition. According to Putirka and Rarick (2019), these mineral assemblages can be classified as quartz-bearing pyroxenites (Table 3).

We can compare them with the results proposed by Brown and Elkins-Tanton (2009) and Malavergne et al. (2010). In order to describe the internal structure of Mercury, Malavergne et al. (2010) use p-MELTS to model the CB ideal bulk silicate composition (similar to our Model 2). Their modeling covers a pressure range of 1–6 GPa, and temperature range of 1473–2473 K. Two different scenarios have been investigated in their work: a first one with crystallization of a magma ocean and a second one without. The latter scenario predicts a mantle composed of major orthopyroxene, with significant amounts of clinopyroxene and quartz at any pressure, while garnet becomes stable at *P* > 2 GPa and plagioclase is stable at 1 GPa.

The former scenario results to be dominated by orthopyroxene at *T* > 1773 K, with possible garnet at high pressures, clinopyroxene and silica polymorphs. However, we note some differences:

1. garnet is absent in Malavergne et al. (2010) below 3 GPa, while it is present in our calculations;
2. spinel is present in minor amounts in Malavergne et al. (2010), while it is absent in our calculations;
3. clinopyroxene is present at all pressures in Malavergne et al., while our amount of Cpx is very low (see Tables in Supporting Information S1). Our model hence tends to stabilize garnet over clinopyroxene;

4. liquid is not present in Malavergne et al. (2010) model, because they do not include this in the calculations, given the poorly constrained EOS of the silicate liquid phase at $P > 3$ GPa (see p. 202 of the paper for further details).

Nevertheless, our results are in general agreement with Malavergne et al. (2010) and Brown and Elkins-Tanton (2008), where the minerals predicted to be stable at pressures ranging from 2 to 7 GPa are quartz, garnet, clinopyroxene, and plagioclase.

Model 5 and Model 6 are both based on Indarch (EH4)-chondrite bulk mineralogy. These two mineral assemblages are both dominated by orthopyroxene (i.e., enstatite), clinopyroxene and variable amounts of quartz. Therefore, considering the scheme proposed by Putirka and Rarick (2019), these mineral assemblages can be classified as quartz-bearing pyroxenites (Table 3).

A very similar bulk composition has been already modeled by Malavergne et al. (2010). They described two different mineral assemblages, as mentioned in the previous paragraph. If no magma ocean crystallization is assumed to have occurred, orthopyroxene is the dominant phase, followed by clinopyroxene and quartz at all pressures, while plagioclase is stable at lower pressures (<3 GPa).

Otherwise, if the post-magma ocean crystallization scenario is considered, in addition to other phases mentioned above, garnet becomes stable at higher pressures. In the same range of pressures investigated by our modeling, this model predicts the stability of quartz, coesite (at higher pressures) and clinopyroxene, while our Model 5 and Model 6 also predict orthopyroxene, which becomes stable at 1873 K in the post-magma ocean crystallization scenario, and garnet, which is shown to be stable at pressures higher than 5 GPa.

In light of the above, we can conclude that olivine- free mantles are significantly enriched in silica polymorphs. This could result in a lower melting point and greater melt production respect with low silica-enriched bulk silicate compositions (e.g., Model 2 shows larger amounts of melt respect with Model 3).

5.4. Correlations Between Mantle and Crust Composition

The three main different mantle assemblages described above might potentially lead to different crustal compositions as a result of partial melting. The mantle mineralogy proposed in Model 1 was based on the same CH-bulk composition proposed by Anzures et al. (2020). These authors predicted a mantle dominated by enstatite (as for our Model 1) and found that lavas in Northern Smooth Plains on Mercury show the same composition of the CH bulk composition-derived melt. Therefore, the putative lavas derived from the melting Model 1 proposed in this work are thought to agree with their melting experiments, except for the sulfur speciation. However, according to Anzures et al. (2020), we can argue that dominant crustal S-species could be (Mg, Ca)S, Na_2S, or CaS, depending on the estimated value of fO_2. Brown and Elkins-Tanton (2008) offered a solidification model of the putative magma ocean of Mercury, describing also the primitive crustal composition. As illustrated also in Section 4.2, the Model 2 mantle is based on the same CB averaged bulk composition presented in Brown and Elkins-Tanton (2008). The predicted Mercury's ancient crust mineral composition, formed after a CB-derived magma ocean solidification, is variable according to its iron content. The formation of a flotation crust depends on its lower density compared to the magma ocean. Our modeled bulk composition has an iron abundance of <3%, so no flotation crust can form, as shown by Brown and Elkins-Tanton (2008). Lavas would be produced by adiabatic melting during the mantle solid-state overturn (Brown & Elkins-Tanton, 2009). Its estimated thickness is < 10 km. The predicted mineralogy consists of major quartz and feldspars (mainly albitic in composition), clinopyroxene, and forsterite (Brown & Elkins-Tanton, 2009). On the contrary, if the magma ocean would be enriched in iron, a quartz flotation crust would form. This could not occur in a magma ocean modeled from Model 3, since it has a lower abundance in silica. Malavergne et al. (2010) predicted a composition of Mercury's lavas dominated by orthopyroxene, plagioclase, quartz, and minor clinopyroxene, in agreement with our results and those reported by Brown and Elkins-Tanton (2009). Finally, we consider the crustal compositions that could be derived from Model 5 (enstatite-like bulk composition) and Model 6 (enstatite-like bulk composition, depleted in SiO_2). Malavergne et al. (2010), for such composition, describe a Mercury's crustal mineralogy dominated by enstatite, plagioclase, quartz, and possible clinopyroxene.

A comprehensive resume of the putative earliest crustal compositions for our additional models (Compositions 1, 2, 3, 4) is offered by Brown and Elkins-Tanton (2009) and Malavergne et al. (2010). Brown and Elkins-Tanton (2009) described that, after the magma ocean stage, no flotation crust was formed, if a heterogeneous mantle

was assumed in modeling. Differently, if Composition 2 (Morgan & Anders, 1980) was representative of a homogenous bulk mantle, the formation of a flotation crust occurred, and a thicker igneous early crust originated (~30 km). Malavergne et al. (2010) proposed for the same bulk composition adopted in our Composition 1 (Goettel, 1988) and Composition 3 (Taylor & Scott, 2003) a crustal mineralogy formed by plagioclase, pyroxene, and quartz. Our model of Composition 4 (Taylor & Scott, 2003—high metal) would result in a crust composed of olivine, pyroxene, and plagioclase, according to these authors.

On Earth, pyroxenites-derived melts are thought to contribute to a significant proportion of the total melt produced in the upper mantle, since pyroxenites have a lower solidus temperature and higher melt productivities than peridotites (Hirschmann & Stolper, 1996; Lambart et al., 2009, 2012; Pertermann & Hirschmann, 2003). A consequence of a lower solidus temperature (Ts) in the upwelling mantle is that melting begins 15–25 km deeper than peridotite (solidus estimated at P less than about 30 kbar, Hirschmann & Stolper, 1996). A pyroxene-dominated mantle would melt at greater depth than peridotites, with a higher production rate (see also Figure 10). Our calculations revealed that pyroxene dominated mantles tend to melt at lower temperatures (~1550 K for Model 2) and producing larger volumes of melt (>70 vol.%). For further details in modeling, please refer to Methods section. Interestingly, all the potassium stored in the bulk compositions studied, is stocked in melt and not in solid phases. This could lead to a peculiar distribution of radiogenic K, involved in internal heating processes.

It is reasonable to infer crustal compositions of exo-Mercuries by comparison with Mercury. Surface Mercury lavas may possess komatiitic or boninitic (Charlier et al., 2013; Stockstill-Cahill et al., 2012; Vander Kaaden et al., 2017; Vander Kaaden & McCubbin, 2015, 2016), high-Mg basaltic (Stockstill-Cahill et al., 2012) or noritic-gabbroid compositions (Stockstill-Cahill et al., 2012). These heterogeneities reflect the existence of at least two distinct mantle sources (Charlier et al., 2013). The first is a more fertile, lherzolitic source, while the second is a depleted harzburgitic source. The compositions derived from the extrusion of these magmas are high-Mg lavas of high magnesium regions (HMR terrains) and intermediate Mg-rich lavas (Weider et al., 2015). Both compositions require high temperature (>1500°C) to erupt. Likewise, Mercury's lavas require high degree of melting and high extraction rates. However, olivine abundances on surface are too low to be compatible with komatiitic lavas (Charlier et al., 2013; Stockstill-Cahill et al., 2012). A boninitic composition has been suggested from experiments simulating magma formation at Mercury mantle conditions, assuming a mineral assemblage dominated by olivine, with minor pyroxenes and plagioclases (Vander Kaaden & McCubbin, 2015).

A mantle rich in pyroxenes, such as described by our models, could potentially explain the high melt productivity (e.g., 5 to > 10 times the pyroxenite proportion in the melt source; Pertermann & Hirschmann, 2003) needed for the high degree of partial melting required for Mercury's lavas emplacement (Namur, Collinet, et al., 2016). Moreover, the lower solidus shown by pyroxenites could agree with the high depth of mantle source predicted to have formed high-Mg IpC-HCT on Mercury (Intercrater Plains and Heavily Cratered Terrains; Namur, Collinet, et al., 2016).

6. Implications

In this Section, several implications, deduced from the results, will be addressed. They are not based upon new findings but offer a more complete prospective about reduced exoplanets as whole system.

6.1. Implications for the Core: Size, Composition, and Dynamics

The mantle mineralogy, composition, and structure of a planet's core are closely linked in terms of evolution, volatile exchange, dynamic processes, and activity (Trønnes et al., 2019 and references therein). In particular, the CMB layer strongly affects the core composition (Litasov & Shatskiy, 2016 and references therein). Furthermore, the global convection of a planet also plays a fundamental role in the core evolution (Olson et al., 2015). Therefore, reduced mantles necessarily influence their respective cores. Our modeling, according to previous literature, has shown that planets originated by accretion of CB-EN and other reduced materials, such as Mercury and analog exoplanets, display a mantle rich in pyroxene, differently from what is observed in other rocky planets' mantles. First, it has been considered that a pyroxene-rich mantle may show a more vigorous mantle convection. This evidence could affect the core evolution since the CMB heat flow in a global circulation mantle depends on the temperature at CMB and transport properties (e.g., viscosity, thermal conductivity, Olson et al., 2015). The inner core nucleation is also indirectly affected by the heat flow at CMB because its timing is related to the heat

flow. Also, the lower temperature of the solidus of this pyroxenitic mantle may have repercussions on the core, since the depth required for melting is greater than for a peridotitic mantle, potentially lying at CMB (Pertermann & Hirschmann, 2003).

6.1.1. Size of Reduced Cores

Unlike the olivine-dominated mantle, characterized by an average density value of 3,500 kg m^{-3}, the pyroxenes - rich mantles modeled in this study exhibit maximum density values always ranging between 3190.5 and 3323.2 kg m^{-3}. It should be noted that these densities may be partially overestimated since these densities did not consider less dense minerals such as MgS or CaS, which are not included in the database used to perform thermodynamic calculations. Therefore, we predict that our densities for S-bearing mineral assemblages could be lower than 3,030 kg m^{-3} (Knibbe et al., 2021). A pyroxene-dominated mantle requires a denser and consequently smaller core since it is less dense (Lark et al., 2022).

6.1.2. Composition and Dynamics of Cores Coupled With Reduced Mantles

A mantle equilibrated under reducing conditions, with a thickness comparable to that of Mercury ($\approx$400 km, Tosi et al., 2013), would not display significant phase transitions among minerals, except for the pyroxene-to-garnet transition (Riner et al., 2008). Consequently, the mantle-core interface may exhibit less geochemical complexity. We noted that, on Earth, the complexity of this interface is especially related to plate tectonics (slab recycling) and metals-silicates reactions.

The strong heterogeneity displayed at Earth's CMB, confirmed by geochemical, mantle convection and seismological studies (Nakagawa & Tackley, 2004b; Tackley, 2002), may not characterize the CMB of sub-Earths, due to the absence of compositional anomalies above this layer, such as the number of lateral heterogeneities in the D″ region (Olson et al., 2015; Tackley, 2002). The absence of a compositionally dense layer above the CMB, which might reduce the rate of cooling in the core, could imply an enhanced core freezing process, resulting in a too low heat flux to drive the geodynamo (Nakagawa & Tackley, 2004a). It is important to note that, for Mercury, the existence of a FeS layer laying at the top of the core has been proposed (Hauck et al., 2013; Malavergne et al., 2010; D. E. Smith et al., 2012) and would be characterized by a lower density with respect to the outer core. Assuming the existence of this lower density layer, the dynamo could be weaker than predicted. The FeS layer hypothesis will be briefly discussed in Section 6.1.2.1. However, a lateral heterogeneity is assumed to exist in Mercury's mantle since that crustal rocks are supposed to be formed from magmas deriving from almost two different mantellic sources (Charlier et al., 2013; Weider et al., 2012). In this case, the core freezing could be limited by this mantle heterogeneity, as the heat flow from the core would be larger (Olson et al., 2015 and references therein).

Finally, assuming this mantle to be anhydrous and the reduced environment, there are no mantle phases carrying water, resulting in the core not being enriched in H or O. Therefore, the only light elements that could enter the core to form alloys with Fe are Si, S, C, and to a lesser extent, N, P, and Cl, all possible candidates in Earth core as light elements (Litasov & Shatskiy, 2016). Simultaneously, if the volumetric fraction of the core in a sub-Earth is similar to that measured for Mercury, it is reasonable to anticipate some compositional variability within such a sizable core.

6.1.2.1. Implications for the Core Composition: The Role of Sulfur

Sulfur is a light element that is believed to have been incorporated into Earth's core, with an amount of approximately 2 wt. % estimated from cosmochemical observations (Kilburn & Wood, 1997; Litasov & Shatskiy, 2016). However, experiments performed at Earth-pressure and temperature conditions suitable for a core-segregation in a deep magma ocean revealed that sulfur may not act as highly siderophile element at high P-T. This further indicates that sulfur does not represent a dominant light element in the terrestrial core (Suer et al., 2017).

When modeling the sulfur content in the cores of sub-Earths, it can be beneficial to consider various hypotheses derived from studies conducted on Mercury. The role of sulfur has been extensively investigated for this planet, given the high sulfur content assumed to be present in its mantle ($\approx$11 wt. %, Boukaré et al., 2019; Namur,

Charlier, et al., 2016). Several studies have explored the possibility of the presence of a FeS layer at the top of the outer core (Cartier et al., 2020; Namur, Charlier, et al., 2016; Steenstra & van Westrenen, 2020).

If the bulk sulfur content of proto-Mercury was sufficient (Malavergne et al., 2010; D. E. Smith et al., 2012), the presence of a buoyant sulphide-rich layer, having a variable thickness, depending on initial S-abundance in precursor material, at the top of the core might be realistic, as suggested both by geophysical and experimental data (Chabot et al., 2014; Charlier & Namur, 2019; Malavergne et al., 2010; Namur, Charlier, et al., 2016). This hypothesis was proposed to justify the measured magnetic field, generated by the possible dynamo deriving from the presence of solid layer over a molten core (Hauck et al., 2013; D. E. Smith et al., 2012), whose presence was supported by gravity measurements (Genova et al., 2019; Knibbe & van Westrenen, 2018). This layer would also represent a preferential site of storage for trace elements and other cations (i.e., Ca^{+2}, Mg^{+2}; Anzures et al., 2020). However, more recent studies evidenced that the required S-content for Mercury's core is not so high (Knibbe & van Westrenen, 2018), therefore the FeS layer would be thinner than 90 km, as deduced from titanium measured in Mercury's lavas (Cartier et al., 2020) and sulfur solubility in silicate melt (Namur, Charlier, et al., 2016). Finally, experiments on the sulfur's geochemical behavior at high reducing conditions have revealed its trend to act as lithophile (Kilburn & Wood, 1997; Steenstra, Trautner, et al., 2020), and resulting in the measured high S-content of Mercury's surface (Namur, Charlier, et al., 2016). Several experiments have evidenced that S under highly reducing conditions, preferentially bonds with Mg and Ca, rather than Fe, due to its increased solubility in silicate melts (Berthet et al., 2009; Cartier et al., 2014; Chabot et al., 2014; Ebel & Alexander, 2011; Holzheid & Grove, 2002; Malavergne, Berthet, & Righter, 2007, 2014; McCoy et al., 1999; Namur, Charlier, et al., 2016; Vander Kaaden et al., 2017; Zolotov et al., 2013). The solubility of sulfur in solid iron is low at the pressures and temperatures suggested for Mercury's core (Li et al., 2015), thought to be 1600–3000 K and 5–40 GPa (Rivoldini & Van Hoolst, 2013).

A more sulfide-rich mantle could have a lower density, implying a smaller and denser core, aside from the distribution of sulphides (Lark et al., 2022). A sulphide-free mantle requires a core with a radius Rc = 2006^{+18}_{-19} km and $\rho c = 7234^{+117}_{-108}$ kg m^{-3}, whereas a mantle with 10 wt.% sulfur as extracted (dispersed) sulphides requires a radius Rc = 1973^{+21}_{-22} km and $\rho c = 7558^{+150}_{-138}$ kg m^{-3}, approximately 300 kg m^{-3}denser (Lark et al., 2022).

The presence of sulfur within the core would limit the amount of silicon incorporated into the iron alloy (Chabot et al., 2014; Kilburn & Wood, 1997; Steenstra & van Westrenen, 2020). This sulfur would preferentially accumulate in the outer core, assuming a core structure similar to that of Earth (Litasov & Shatskiy, 2016). The outer core not only possesses a distinct density compared to the inner core but also exhibits a more heterogeneous composition, facilitating not only convection associated with the liquid layer but also compositional convection. Therefore, there could be two distinct dynamo sources. The combination of these two distinct mechanisms leads to enhanced core activity, which should manifest as a stronger magnetic field, which has paradoxically not been described for Mercury (Christensen, 2006).

6.1.2.2. Implications for the Core Composition: The Role of Carbon

Several studies suggest that the core represents the largest reservoir of carbon C on Earth, its abundance is not well constrained, ranging between 0.2 and 4 wt.%, but could be lower (Chi et al., 2014; Dasgupta et al., 2009; Fischer et al., 2020; Litasov & Shatskiy, 2016; Wood, 1993; Wood et al., 2013). This light element would be concentrated in the inner core, forming iron carbide (Fe$_3$C$_7$; B. Chen et al., 2014; Mookherjee et al., 2011). C would affect dynamic, thermal properties, and structure of terrestrial core (Wood et al., 2013). Carbon exhibits a siderophile affinity during mantle-core differentiation (Dasgupta et al., 2013). Therefore, C is a plausible light element in the outer core of a reduced mantle, though most of experiments have been performed at more oxidized conditions respect with those accounted in this paper (e.g., Dasgupta et al., 2013; Fischer et al., 2020).

Considering this, a more realistic composition of Mercury's core requires the presence of other light elements alloying to iron, such as carbon (Edmund et al., 2022; Steenstra & van Westrenen, 2020). Carbon has been suggested to play an important role in Mercury's core formation, originating a possible primary graphitic crust (Steenstra, Trautner, et al., 2020; Vander Kaaden & McCubbin, 2015; Vander Kaaden et al., 2020). A similar graphite-floatation crust has been proposed also for Earth (Keppler & Golabek, 2019), where would reduce the carbon content of the core. Calculations including C alloying indicates that this element reduces the Si content of the core by roughly 1.5–1.8 wt.% per wt. % C, similarly to the effect played by sulfur's presence (Edmund

et al., 2022; Steenstra, Seegers, et al., 2020). The most recent estimations of carbon (C), obtained from the study of low-reflectance materials (LRM; see Lark et al. (2023) for details), suggest that the core of Mercury contains between 0.5 wt.% if it is extremely rich in Si, up to 1–4 wt.% of C, a value in agreement with geodetic data (Knibbe & van Hoolst, 2021). If the mantle and core of Mercury have equilibrated with respect to C, then the core must have preferentially partitioned it, resulting in a reduced quantity of Si in the core. This scenario, where SiO_2 is abundant in the mantle and scarce in the core, promotes the stability of pyroxenes over olivine in the mantle (see Figure 8), consistent with our models described in Section 4.

6.1.2.3. Implications for the Core Composition: The Role of Other Alloying Elements

Since Earth's core is ∼10% less dense than pure iron–nickel under the same pressures and temperatures (Fischer et al., 2020), a variety of light elements has been proposed (S, Si, O, C, H, N, Cl, P; Litasov & Shatskiy, 2016). The light elements are important to determine the melting point of pure iron but specially to drive compositional convection in the outer core, which is essential to generate dynamo. Such light elements must be present also in other planets' cores. Giving the reduced conditions assumed for our sub-Earths cores, several light elements are more realistic to be stored in the outer core than others. In the next sections, we briefly address this question.

6.1.2.3.1. Silicon

Silicon is predicted to be present in Earth's outer core by models of core formation at deep magma ocean's temperature and pressure conditions (Fischer et al., 2015; Hirose et al., 2017; Siebert et al., 2012). The silicon concentration in the outer core changes with fO$_2$ (Fischer et al., 2015; Siebert et al., 2012). At reduced conditions, Si amounts ranges between 8 and 9 wt.%, assuming a fixed fO$_2$ value of –5.9 log units below the IW buffer (Allègre et al., 1995). At more oxidized conditions, the concentration decreases to 2 wt.% (Fischer et al., 2015; Litasov & Shatskiy, 2016; Siebert et al., 2012). As oxygen fugacity decreases, silicon acts as siderophile. Silicon and sulfur are mutually incompatible during core formation (Kilburn & Wood, 1997), so if the oxygen fugacity is sufficiently low to drive silicon entering in the core, sulfur becomes more lithophile, remaining in the silicate melt and then in the mantle.

Considering the reducing conditions that characterize Mercury, silicon is assumed to be a significant light element alloyed with iron to form the outer core (Chabot et al., 2014; Edmund et al., 2022; Steenstra & van Westrenen, 2020; Vander Kaaden et al., 2020). This hypothesis is further supported by geodetic data, which estimate a silicon concentration in the outer core ranging from 7 wt.% to 14 wt.%, depending on the chosen precursor material (Knibbe et al., 2021; Steenstra & van Westrenen, 2020).

6.1.2.3.2. Oxygen

Oxygen is thought to be a constituent of Earth's outer core, together with silicon. The predicted concentration changes with fO$_2$. At oxidizing conditions, the estimate is 5 wt.% (Siebert et al., 2012), while at more reducing ranges between 2 and 4 wt.% (Fischer et al., 2020; Siebert et al., 2012). In the case of Mercury, the availability of oxygen hypothesized is too low to be partitioned in the core. Likewise, we deduced that this light element cannot be present in the outer cores of reduced sub-Earths.

6.2. Geodynamic Implications

Orthopyroxene and clinopyroxene represent the most abundant minerals in each modeled mantle mineralogy when the SiO_2 abundance assumed in the initial bulk composition is >40 wt.% (Figure 6 and Tables S2 and S3 in Supporting Information S1). The dominance of orthopyroxene was also attested in the silica depleted Indarch model (Model 5-depleted), where it was assumed that 20 wt.% SiO_2 had entered the core, consistent with the proportions of silica content for Mercury's core (Edmund et al., 2022; Nittler et al., 2018).

In order to understand the dynamic implications of a pyroxene dominated mineralogy, we have to better characterize the geochemical behavior of different types of rock, having normative orthopyroxene ranges between 40 and 90 (Le Maitre et al., 2002) such as olivine-pyroxenites (i.e., ultramafic plutonic rock, consisting essentially of pyroxene and up to 50% of olivine, Le Maitre et al., 2002), websterites (i.e., a variety of pyroxenite consisting of equal amounts of clinopyroxene and orthopyroxene, Le Maitre et al., 2002) and orthopyroxenites (i.e., an ultramafic plutonic rock consisting almost entirely of orthopyroxene, Le Maitre et al., 2002). Another remarkable

evidence of our models is the presence of silica polymorphs in these rocks, represented by quartz at low *T-P* and coesite at high *T-P* (Figure 6 and Tables S2 and S3 in Supporting Information S1). These results are consistent with the mineralogy modeled for Mercury's mantle in Malavergne et al. (2010), who assumed as precursor materials EN (Berthet et al., 2009 bulk composition) and CB chondrites (Brown & Elkins-Tanton, 2008 bulk composition). They performed their thermodynamic calculations by using p-MELTS (Ghiorso & Sack, 1995), but the results of our Model 2 (CB ideal composition, our benchmark) and our Model 5 (EN) are comparable. Putirka and Xu (2021) obtained quartz-normative ultramafic rocks for mantles of exoplanets deduced from polluted white dwarfs compositions and they proposed a new nomenclature for these exotic rocks (see Table 1 of this paper for more information). We could define our modeled mineralogy as quartz-bearing pyroxenites, because our amounts of quartz are slightly lower respect with those reported in Putirka and Xu (2021). However, this evidence has important repercussions on the rheology and therefore on the convective regime of the sub-Earths since the orthopyroxene may have different rheological properties than olivine (e.g., viscosity, Yamamoto et al., 2008; Hansen & Warren, 2015; Bystricky et al., 2016). If orthopyroxene had a lower solidus temperature, a lower viscosity, and a lower strength than olivine, the mantle dynamic could be quite different from the terrestrial one, which is ruled by peridotites properties.

Putirka and Rarick (2019) have already argued that exoplanets mantellic mineralogy might be quite different from Earth, discussing about the existence of pyroxene-rich planets. Moreover, the redox state of the mantle could also affect the resulting rheology, modifying the minerals' strength (Hitchings et al., 1989; Ji et al., 2001), especially Fe-bearing phases rheological parameters are modified by the oxygen fugacity of the system (e.g., magnetite/iron described in Hitchings et al. (1989)).

The rheological properties and deformation mechanisms of pyroxenitic rocks have been scarcely investigated (Avé Lallemant, 1978; Avé Lallemant et al., 1980; Boland & Tullis, 1986; Mackwell, 1991; Ranalli, 1995). Recent works describe the dislocation creep mechanism in clinopyroxene aggregates, involving water (S. Chen et al., 2006; Hier-Majumder et al., 2005; Zhang et al., 2017). There is no general agreement regarding certain rheological properties of these minerals. For instance, some studies reported a higher viscosity of olivine compared to pyroxene (Ranalli, 1995, 1997), while others consider orthopyroxene to be more viscous by several orders of magnitude than olivine (Hansen & Warren, 2015; Yamamoto et al., 2008). The same uncertainty is found in the difference in strength, with some suggesting that olivine exhibits greater strength than orthopyroxene (Ji et al., 2001; Ohuchi et al., 2011; Raleigh et al., 1971), while others proposed that orthopyroxene possess a greater strength than olivine (Hansen & Warren, 2015; Lawlis, 1998; Mackwell, 1991; Ross & Nielsen, 1978; Yamamoto et al., 2002, 2008). Lawlis (1998) investigated the rheology of Al-free and Fe-bearing clinoenstatite and protoenstatite and he concluded that log of deformation ($\dot{\varepsilon}$) varies linearly with enstatite fraction, under conditions favorable for dislocation creep. So, the activation energy (Q) increases linearly with the orthopyroxene fraction. He also supposed that differences in strength, between olivine and orthopyroxene, could be explained by protoenstatite-orthoenstatite differences in rheological properties.

Likewise, several papers, which confirmed that orthopyroxene shows a greater strength than olivine (Hitchings et al., 1989; Mackwell, 1991) described the rheological properties of proto-enstatite, as underlined by Ohuchi et al. (2011), which could be greater than orthoenstatite. Furthermore, the methodology adopted by Hitchings et al. (1989) and Mackwell (1991) is also challenged by Ohuchi et al. (2011), therefore it is difficult to outline if pyroxene is effectively stronger than olivine.

Yamamoto et al. (2008) performed in situ measurements of the yield strength of olivine, orthopyroxene, and Cr-spinel at a fixed range of *T* (400–600°C) and P (up to 10 GPa) and found that olivine is always the weakest mineral. Orthopyroxene is stronger than olivine and spinel at 10 GPa- 700°C. Conversely, Ohuchi et al. (2011) found that orthopyroxene, at a pressure and temperatures typical of terrestrial lithosphere, is weaker than olivine, at any experimental conditions. Moreover, this paper suggests that the addition of orthopyroxene in lithosphere results in its reduced strength.

These contrasting results affect the resulting crust strength: an orthopyroxene dominated lithosphere would be strong than an olivine-rich one, resulting in a more difficulty in undergo plate tectonic-related processes, such as rifting (Putirka & Rarick, 2019), if it assumed that orthopyroxene is stronger and more viscous than olivine (Yamamoto et al., 2008). When it is considered that orthopyroxene presence leads to a weaking in lithosphere's strength, the resulting behavior may be different (Ohuchi et al., 2011).

6.2.1. Rheology of Pyroxene-Dominated Mantles

In the next sections, we consider that reduced mantles, characterized by an abundance of pyroxenes, may give rise to distinct convective and tectonic activity. Due to the lack of consensus among authors regarding the differing viscosities of olivine and pyroxenes, we adopted the assumption that pyroxenes possess a lower viscosity compared to olivine, as suggested by Ranalli (1995, 1997), and Ohuchi et al. (2011). Given that Ohuchi et al. (2011), have thoroughly scrutinized the prior literature based on the methodology employed to estimate the viscosity of olivine and pyroxenes (refer to Section 6.2.1.1), we believe the results provided by this article to be the most robust.

6.2.1.1. Viscosity of Pyroxenes-Rich Lithologies

Creep rates in mantellic rocks depend on the composition of rocks, temperature, presence of water and to a lesser extent the hydrostatic pressure (Lawlis, 1998 and reference therein). Moreover, the strength of the lithosphere is one of the key factors which drives the convection style in a planet (Ohuchi et al., 2011 and reference therein). Consequently, a mantle mineralogy that features orthopyroxenes (i.e., enstatite) as the most abundant mineral, followed by lesser amounts of clinopyroxene and potentially olivine, could lead to a convective regime significantly different from that modeled for Earth, Mars, or Venus, where the rheological behavior is driven by peridotites. Previously, the creep strength of olivine has been used in estimating the strength of the lithosphere (Kohlstedt et al., 1995). Recently, several studies have instead enhanced the importance of pyroxene-bearing lithologies in controlling the rheology of terrestrial lithosphere and related magmatogenesis (Lambart et al., 2016; Ohuchi et al., 2011).

We assumed that dislocation creep is the dominant mechanism which drives deformation in thin mantles, as sub-Earths mantles (Lawlis, 1998 and reference therein). We also adopted the assumption that pyroxenes exhibit lower viscosity and lower strength than olivine (Ohuchi et al., 2011; Ranalli, 1995).

We use for dislocation creep the flow law written as:

$$\dot{\varepsilon} = A \frac{\sigma_d^n}{d^p} \exp\left(-\frac{Q}{RT}\right), \tag{1}$$

where A is a parameter, σ_d is the differential stress, n is the stress exponent, d is the grain size, p is the grain size exponent, Q is the activation energy for creep and R is the gas constant (8.314 J mol^{-1} K^{-1}). The effective viscosity is written as:

$$\eta_{eff} = \frac{\sigma}{2\dot{\varepsilon}}, \tag{2}$$

where σ is the deviatoric stress and $\dot{\varepsilon}$ is the deviatoric strain rate. For dislocation creep, the effective viscosity indicated with a caron symbol is written as (Gerya, 2019, p. 77):

$$\check{\eta}_{eff} = \frac{1}{2^{\frac{n-1}{n}}3^{\frac{n+1}{2n}}} \frac{1}{A^{\frac{1}{n}}d^{\frac{p}{n}}(\dot{\varepsilon})^{\frac{n-1}{n}}} \exp\left(\frac{Q}{nRT}\right) \tag{3}$$

By using Equation 1, we produced data plotted in Figure 9. Table 4 presents the adopted rheological data for dislocation creep for dry forsterite, orthopyroxene and clinopyroxene.

The viscosity dependence on temperature shown in Figure 9 is of particular interest, as the Rayleigh number (Ra) depends inversely on the viscosity:

$$Ra = \frac{\rho g \alpha \Delta T d^3}{\eta \kappa} \tag{4}$$

where ρ is the density, g is the gravitational acceleration, α is the thermal expansivity, ΔT is the temperature variation, d is the layer thickness, η is the viscosity, κ is the thermal diffusivity.
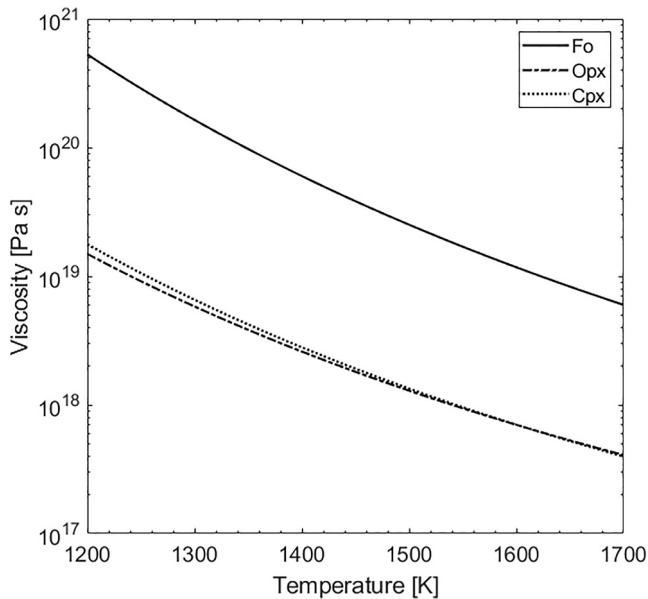
Figure 9. Viscosity dependence on temperature of forsterite *(Fo)*, orthopyroxene *(Opx)*, and clinopyroxene *(Cpx)* assumed for sub-Earths reduced mantles. The symbology of curves is reported in the legend.

These calculations indicate that, if mantle viscosity decreases, mantle convection will be more vigorous. Therefore, a pyroxene-rich mantle, characterized by a lower viscosity, such as reduced sub-Earths mantles, will yield a stronger convection. If the inner regions of stellar nebulae are characterized by pyroxene-rich mantle, it could be argued that inner planets are more active than the other terrestrial planets.

6.3. Solidus Temperatures of Pyroxene-Rich Rocks

Pyroxenes-rich rocks are also suggested to have a lower solidus temperature than peridotites (Gerya, 2019; Green & Ringwood, 1967; Lambart et al., 2009; Pertermann & Hirschmann, 2003; Yasuda et al., 1994; Yaxley & Green, 1998). Experiments conducted on basaltic pyroxenite show a solidus temperature at ≈3 GPa of 1310°C ± 12°C, while the liquidus temperature is posed at 1500–1525°C (Pertermann & Hirschmann, 2003). Figure 10 shows the solidus curves extrapolated from each model. Pyroxene-rich mineral assemblages start to melt at lower T (<1800 K) than olivine-rich models and tend to have higher production rates.

Consequently, in a mantle dominated by pyroxenes, the onset and sustained convection over time may be more easily achievable than in a lherzolitic mantle. It is also assumed that even a mantle characterized by thinner layers can exhibit convection, provided it is orthopyroxene- rich.

If the viscosity of orthopyroxene is lower than olivine viscosity (see Section 6.2.1.1), the dynamic activity of the resulting mantle could be different. The presence of pyroxenes would have facilitated a longer-lasting convective activity, resulting in certain mantle regions remaining molten for an extended period of time, even though the melt productivity may have declined over time, consistent with the findings of relatively recent volcanic activity on Mercury, documented from Caloris Basin pyroclastic deposits.

In light of the above, if we assume that orthopyroxene is characterized by lower viscosity (Ranalli, 1995, 1997), lower strength (Ohuchi et al., 2011) and lower solidus temperature, the lithosphere of sub-Earths could undergo a different dynamic activity and evolution in time with respect to a peridotite rich mantle as the terrestrial mantle.

New experimental evidence on the rheological properties and deformation behavior of pyroxenitic mantle rocks under anhydrous conditions and at various redox states is urgently needed to understand not only the dynamics of extraterrestrial mantles but also the lithosphere of the Earth, where orthopyroxenes could play a key role in the initiation of tectonics (Ohuchi et al., 2011).

6.4. Distribution of Radiogenic Heat Sources: ^{40}K, ^{232}Th, ^{238}U, ^{235}U

The concentration of Heat Producing Elements (HPE) in terrestrial mantles plays an important role in determining the total heat production of a planetary body, affecting its thermochemical evolution.

Boujibar et al. (2019) evidenced as U ad K partition into liquid FeS but not liquid Fe-Si at relevant Mercury's internal conditions. Recent experiments conducted on synthetic composition resembling Mercury's silicate fraction shown that heat-producing elements (U, Th and K) become less lithophile at low oxygen fugacity values (∼IW − 1 to ∼IW − 8). However, Pirotte et al. (2023) discuss that Th behaves as lithophile at all fO_2 values investigated (∼IW − 2 to ∼IW − 6) and is ∼20 times less chalcophile than U.

However, if we assume that a small portion of the potassium present in our bulk compositions is ^{40}K (0.0120%), we can try to define how it is distributed (see Tables S2 and S3 in Supporting Information S1). Potassium is almost all stored in clinopyroxene phases at low P and T for Models 1, 3, 4, 5, 6. K-feldspar is predicted in Model 2 at lower pressure and temperature. At high pressure and temperature, potassium is stored in the melt for Model 2 and in

Table 4
Rheological Parameters for Dislocation Creep for Dry Forsterite (Kirby & Kronenberg, 1987), Orthopyroxene and Clinopyroxene (Ranalli, 1995, 1997)

	A (MPa^{-n} s^{-1})	p	n	Q (kJ mol^{-1})
Forsterite	6.3×10^4	0	3.5	533
Orthopyroxene	3.2×10^{-1}	0	2.4	293
Clinopyroxene	15.7	0	2.6	335

clinopyroxene for others (see Table S2 and S3 in Supporting Information S1). If we increase the modeling temperatures, potassium will be concentrated in the "melt" phase for the other models as well. It should be noted that our modeling, lacking S-phases, could only provide a partial description of K distribution in silicates.

The difference between the two models relies probably on the absence of clinopyroxene in Model 2, so, all K goes into K-feldspar, which melts at 1700 K, and we found K in melt phase. In light of this, we infer that potassium is enriched in low density phases, such as feldspar and clinopyroxene and tend to be stored into the crust. However, some K is stock into clinopyroxene also at higher T and P, that is, deeper in the mantle assemblage of Model 6. Melt composition is given by Ca, K and Ti plus SiO_2 and Al for Model 2. The presence of potassium in melt suggests that lavas for this kind of mantle assemblage are enriched in K.

6.4.1. Heating Sources in Reduced Sub-Earths Cores

It is generally assumed that radioactive heat production in the core is negligible (e.g., for Earth, Nakagawa & Tackley, 2004a). For example, high-pressure partition experiments on U indicated that heat production in the core is negligible (Malavergne, Tarrida, et al., 2007). However, the role of ^{40}K in driving the heat flux at Earth's CMB has been recently reevaluated (Gessmann & Wood, 2002; Labrosse, 2003). Geochemical constraints and high-pressure-partition experiments also indicate that the presence of potassium is related to the presence of sulfur in the core (Boehler, 1993; Bouhifd et al., 2007). It is hypothesized that the core of Mercury contains a certain quantity of sulfur (<1.5 wt.%, Namur, Charlier, et al., 2016). If this assumption is also applied to the cores of sub-Earths, the effect of internal heating resulting from potassium (K) should be considered. However, recent experiments conducted by Pirotte et al. (2023) at Mercury's crust-mantle conditions revealed that U, K, and especially Th are concentrated in the BSM (bulk-silicate Mercury) and did not partition in the core, since they are chalcophile at low fO_2 conditions. New experiments performed at high pressure and high temperature and reduced conditions, indicated that HPE preferentially segregates in sulfides than metals (Boujibar et al., 2019).

6.5. Implications for Mercury

Mercury, being the most reduced planet in our solar system (Cartier & Wood, 2019 and references therein), is characterized by a high metal/silicate ratio, as indicated by its high density, the low abundance of FeO on its surface, and the inferred presence of Mg and Ca sulfides (Nittler et al., 2011; Weider et al., 2012, 2014). Various precursor materials have been proposed to describe its bulk composition (Anzures et al., 2020; Brown & Elkins-Tanton, 2009; Cartier et al., 2022; Malavergne et al., 2010; Nittler et al., 2018; Steenstra & van Westrenen, 2020). However, as argued by Chabot et al. (2014), a single bulk composition may not be sufficient to capture the complexity of this planet.

Nevertheless, our mantle modeling for sub-Earths can be extended to Mercury for several reasons. First, we employed the same pressure and temperature range suggested for Mercury in our thermodynamic calculations. In addition, the use of entirely reduced oxides as input can be considered a valid strategy for representing the mantle of Mercury, where core segregation has occurred. Furthermore, our models were based on reduced materials chosen as analogs of Mercury (see Section 3).

Recently, Knibbe et al. (2021) described interior structure models of Mercury constrained by geodetic measurements of the planet (e.g., obliquity and libration), by assuming the presence of a liquid outer core composed of Fe-Si-C. Then, the authors combined the resulting mantle densities with distinct values of the normalized moment of inertia (I) estimated for Mercury and deduced the radius and composition of the core coupled to such mantles. When we combined our resulting mantle densities with the values of moment of inertia suggested by Knibbe et al. (2021), we found that Model 1 (CH bulk composition), Model 2 (CB bulk composition), Model 4 (aubrite bulk composition), Model 5 (EN bulk composition), Model 6 (EN depleted), showing a density between 3,150 and 3,350 kg m^{-3}, could be related to a normalized moment of inertia (I) of 0.3458. The expected core has a radius of 1,973–2,025 km and a putative composition of metals plus 11 wt. % Si (if S and C are present). Silicon contents increase to 14 wt.% if other light elements are absent (Lark et al., 2022). The silicate shell of Mercury has a putative thickness ranging between 470 and 524 km. None of our models show a density >3,350 kg m^{-3}, consequently, we do not expect a value of I: 0.3593, or core radius >2,025 km, with a silicon abundance of about 17 wt.% (plus S and C).
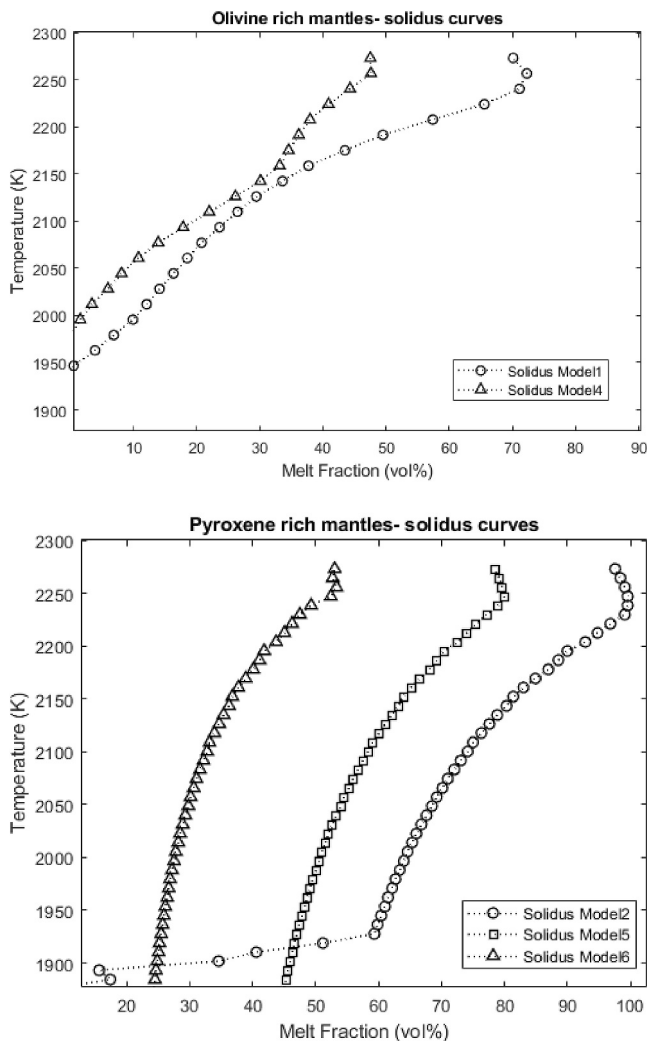
Figure 10. Solidus curves for olivine-rich mantles (upper panel) and pyroxene-rich mantles (bottom panel). The symbology for each curve is indicated in legend.

It should be noted that a pyroxenitic mantle could result in a thermochemical evolution of the planet that differs significantly from previous assessments (Michel et al., 2013; Padovan et al., 2017; Redmond & King, 2007; Tosi et al., 2013). These models were all based on a dry olivine mineralogy of the mantle, and both diffusion and dislocation creep deformation mechanisms are simulated (Redmond & King, 2007).

As discussed in Section 6.2.1, orthopyroxene and clinopyroxene show different rheological parameters for dislocation creep in peridotites (Ranalli, 1997), resulting in the lower viscosity which characterizes a pyroxene-rich mantle; and hence will result in a more vigorous mantle convection.

If this scenario can be extended to the mantle of Mercury, then its convective activity would not only have been more vigorous but also prolonged enough to accommodate the required emplacement times for the volcanic plains. Furthermore, a large-amplitude mantle convection would be consistent with the high degrees of partial melting indicated by the Mg-rich compositions on the surface (Stockstill-Cahill et al., 2012; Vander Kaaden & McCubbin, 2016).

7. Conclusions

We explored the phase assemblages that may constitute mantles of the sub-sized Earth exoplanets located in the inner regions of other stellar systems. We assumed that they formed under more reducing geochemical conditions with respect to Earth, as deduced from the chemical properties of very primordial materials, such as EN, CB, and CH chondrites, which aggregated in poorly oxidized environments. Using Perple_X thermodynamic modeling, we found that the mineralogy of rocky mantles (assuming a dry scenario) would be dominated by pyroxenes instead of olivine, following the SiO_2 abundances in the assumed precursor materials. In a future endeavor, we plan to delve into the modeling of sulfur-bearing minerals, a facet that has not been addressed in this current paper. We identified the phases constituting mantles: orthopyroxene, clinopyroxene, possible minor olivine, garnet, and silica polymorphs; over a range of SiO_2 abundances suggested for the reduced meteorites assumed as precursor materials. We found that reduced mantles in exoplanets would be pyroxene-rich. Since pyroxenes have a lower solidus temperature and lower viscosity as compared to olivine, the mantle activity is predicted to be more vigorous and prolonged in time. Reduced mantles could be more active than terrestrial mantles. Consequently, mantle mineralogy dominated by olivine, which is typical for Earth, may not apply to the reduced-chemistry mantles of sub-Earths and, more broadly, to Mercury. We proposed that the evidence reported in this study for mantles with reduced chemistry could also apply to Mercury since reduced chemistry has been also suggested for Mercury in our solar system (e. g., Cartier & Wood, 2019; Malavergne et al., 2010; Namur, Charlier, et al., 2016; Zolotov et al., 2013 and references therein).

Future analyzes and measurements obtained from the BepiColombo mission will provide new insights which could validate these hypotheses. Furthermore, these data may be extended to exoplanets formed in analog reduced environments. The prospective identification of further exoplanets and the potential mitigation of observational biases would prove advantageous in evaluating these findings.

Data Availability Statement

Data that may be used to reproduce the results in this study is provided as a datafile stored in a Zenodo repository (Cioria et al., 2024). In this repository, the employed thermodynamic database and the input files used to produce results can be found. Further details are reported in Section 2 and in Tables S1 and S1A of Supporting Information S1.

References

Allégre, C. J., Poirier, J. P., Humler, E., & Hofmann, A. W. (1995). The chemical composition of the Earth. *Earth and Planetary Science Letters*, *134*(3–4), 515–526. https://doi.org/10.1016/0012-821x(95)00123-t

Anzures, B. A., Parman, S. W., Milliken, R. E., Namur, O., Cartier, C., & Wang, S. (2020). Effect of sulfur speciation on chemical and physical properties of very reduced mercurian melts. *Geochimica et Cosmochimica Acta*, *286*, 1–18. https://doi.org/10.1016/j.gca.2020.07.024

Avé Lallemant, H. G. A. (1978). Experimental deformation of diopside and websterite. *Tectonophysics*, *48*(1–2), 1–27. https://doi.org/10.1016/0040-1951(78)90083-5

Avé Lallemant, H. G. A., Mercier, J. C., Carter, N. L., & Ross, J. V. (1980). Rheology of the upper mantle: Inferences from peridotite xenoliths. *Tectonophysics*, *70*(1–2), 85–113. https://doi.org/10.1016/0040-1951(80)90022-0

Barrat, J. A., Zanda, B., Jambon, A., & Bollinger, C. (2014). The lithophile trace elements in enstatite chondrites. *Geochimica et Cosmochimica Acta*, *128*, 71–94. https://doi.org/10.1016/j.gca.2013.11.042

Batalha, N. M., Borucki, W. J., Bryson, S. T., Buchhave, L. A., Caldwell, D. A., Christensen-Dalsgaard, J., et al. (2011). Kepler's first rocky planet: Kepler-10b. *The Astrophysical Journal*, *729*(1), 27. https://doi.org/10.1088/0004-637X/729/1/27

Batalha, N. M., Rowe, J. F., Bryson, S. T., Barclay, T., Burke, C. J., Caldwell, D. A., et al. (2013). Planetary candidates observed by Kepler. III. Analysis of the first 16 months of data. *The Astrophysical Journal - Supplement Series*, *204*(2), 24. https://doi.org/10.1088/0067-0049/204/2/24

Benz, W., Slattery, W. L., & Cameron, A. G. W. (1988). Collisional stripping of Mercury's mantle. *Icarus*, *74*(3), 516–528. https://doi.org/10.1016/0019-1035(88)90118-2

Berthet, S., Malavergne, V., & Righter, K. (2009). Melting of the Indarch meteorite (EH4 chondrite) at 1 GPa and variable oxygen fugacity: Implications for early planetary differentiation processes. *Geochimica et Cosmochimica Acta*, *73*(20), 6402–6420. https://doi.org/10.1016/j.gca.2009.07.030

Best, M. G. (2013). *Igneous and metamorphic petrology*. John Wiley & Sons.

Boehler, R. (1993). Temperatures in the Earth's core from melting-point measurements of iron at high static pressures. *Nature*, *363*(6429), 534–536. https://doi.org/10.1038/363534a0

Boland, J. N., & Tullis, T. E. (1986). Deformation behavior of wet and dry clinopyroxenite in the brittle to ductile transition region. In B. E. Hobbs & H. C. Heard (Eds.), *Mineral and rock deformation: Laboratory studies* (pp. 35–49). AGU. https://doi.org/10.1029/GM036p0035

Bouhifd, M. A., Gautron, L., Bolfan-Casanova, N., Malavergne, V., Hammouda, T., Andrault, D., & Jephcoat, A. P. (2007). Potassium partitioning into molten iron alloys at high-pressure: Implications for Earth's core. *Physics of the Earth and Planetary Interiors*, *160*(1), 22–33. https://doi.org/10.1016/j.pepi.2006.08.00

Boujibar, A., Driscoll, P., & Fei, Y. (2020). Super-Earth internal structures and initial thermal states. *Journal of Geophysical Research: Planets*, *125*(5), e2019JE006124. https://doi.org/10.1029/2019je006124

Boujibar, A., Habermann, M., Righter, K., Ross, D. K., Pando, K., Righter, M., et al. (2019). U, Th, and K partitioning between metal, silicate, and sulfide and implications for Mercury's structure, volatile content, and radioactive heat production. *American Mineralogist*, *104*(9), 1221–1237. https://doi.org/10.2138/am-2019-7000

Boukaré, C. E., Parman, S. W., Parmentier, E. M., & Anzures, B. A. (2019). Production and preservation of sulfide layering in Mercury's mantle. *Journal of Geophysical Research: Planets*, *124*(12), 3354–3372. https://doi.org/10.1029/2019JE005942

Brett, R., & Keil, K. (1986). Enstatite chondrites and enstatite achondrites (aubrites) were not derived from the same parent body. *Earth and Planetary Science Letters*, *81*(1), 1–6. https://doi.org/10.1016/0012-821X(86)90095-6

Brown, S., & Elkins-Tanton, L. T. (2008). Predicting Mercury's ancient crustal composition. In *Paper presented at 39th Lunar and Planetary Science Conference, League City, Texas*.

Brown, S., & Elkins-Tanton, L. T. (2009). Earliest planetary crusts: Constraints on the formation of Mercury and implications for bodies of different sizes. In *Paper presented at 40th Annual Lunar and Planetary Science Conference, The Woodlands, Texas*.

Burbine, T. H., McCOY, T. J., Nittler, L. R., Benedix, G. K., Cloutis, E. A., & Dickinson, T. L. (2002). Spectra of extremely reduced assemblages: Implications for Mercury. *Meteoritics & Planetary Science*, *37*(9), 1233–1244. https://doi.org/10.1111/j.1945-5100.2002.tb00892.x

Bystricky, M., Lawlis, J., Mackwell, S., Heidelbach, F., & Raterron, P. (2016). High-temperature deformation of enstatite aggregates. *Journal of Geophysical Research: Solid Earth*, *121*(9), 6384–6400. https://doi.org/10.1002/2016jb013011

Cameron, A. G. W. (1985). The partial volatilization of Mercury. *Icarus*, *64*(2), 285–294. https://doi.org/10.1016/0019-1035(85)90204-0

Cartier, C., Charlier, B., Boyet, M., Spalding, C., & Namur, O. (2022). A large proto-Mercury as the aubrite parent body. In *Paper presented at Mercury 2022 Conference, Orléans, France*.

Cartier, C., Hammouda, T., Boyet, M., Bouhifd, M. A., & Devidal, J. L. (2014). Redox control of the fractionation of niobium and tantalum during planetary accretion and core formation. *Nature Geoscience*, *7*(8), 573–576. https://doi.org/10.1038/ngeo2195

Cartier, C., Namur, O., Nittler, L. R., Weider, S. Z., Crapster-Pregont, E., Vorburger, A., et al. (2020). No FeS layer in Mercury? Evidence from Ti/Al measured by MESSENGER. *Earth and Planetary Science Letters*, *534*, 116108. https://doi.org/10.1016/j.epsl.2020.116108

Cartier, C., & Wood, B. J. (2019). The role of reducing conditions in building Mercury. *Elements*, *15*(1), 39–45. https://doi.org/10.2138/gselements.15.1.39

Casanova, I., Keil, K., & Newsom, H. E. (1993). Composition of metal in aubrites: Constraints on core formation. *Geochimica et Cosmochimica Acta*, *57*(3), 675–682. https://doi.org/10.1016/0016-7037(93)90377-9

Chabot, N. L., Wollack, E. A., Klima, R. L., & Minitti, M. E. (2014). Experimental constraints on Mercury's core composition. *Earth and Planetary Science Letters*, *390*, 199–208. https://doi.org/10.1016/j.epsl.2014.01.004

Charlier, B., Grove, T. L., & Zuber, M. T. (2013). Phase equilibria of ultramafic compositions on Mercury and the origin of the compositional dichotomy. *Earth and Planetary Science Letters*, *363*, 50–60. https://doi.org/10.1016/j.epsl.2012.12.021

Charlier, B., & Namur, O. (2019). The origin and differentiation of planet Mercury. *Elements*, *15*(1), 9–14. https://doi.org/10.2138/gselements.15.1.9

Chen, B., Li, Z., Zhang, D., Liu, J., Hu, M. Y., Zhao, J., et al. (2014). Hidden carbon in Earth's inner core revealed by shear softening in dense Fe_7C_3. *Proceedings of the National Academy of Sciences*, *111*(50), 17755–17758. https://doi.org/10.1073/pnas.1411154111

Chen, S., Hiraga, T., & Kohlstedt, D. L. (2006). Water weakening of clinopyroxene in the dislocation creep regime. *Journal of Geophysical Research*, *111*(B8), B08203. https://doi.org/10.1029/2005jb003885

Chi, H., Dasgupta, R., Duncan, M. S., & Shimizu, N. (2014). Partitioning of carbon between Fe-rich alloy melt and silicate melt in a magma ocean–implications for the abundance and origin of volatiles in Earth, Mars, and the Moon. *Geochimica et Cosmochimica Acta*, *139*, 447–471. https://doi.org/10.1016/j.gca.2014.04.046

Christensen, U. R. (2006). A deep dynamo generating Mercury's magnetic field. *Nature*, *444*(7122), 1056–1058. https://doi.org/10.1038/nature05342

Cioria, C., & Mitri, G. (2022). Model of the mineralogy of the deep interior of Triton. *Icarus*, *388*, 115234. https://doi.org/10.1016/j.icarus.2022.115234

Cioria, C., Mitri, G., Connolly, J. A. D., Perrillat, J.-P., & Saracino, F. (2024). Mantle mineralogy of reduced sub-Earths exoplanets and Mercury-sized objects [Dataset]. *Zenodo*. https://doi.org/10.5281/zenodo.10824308

Clayton, R. N., & Mayeda, T. K. (1999). Oxygen isotope studies of carbonaceous chondrites. *Geochimica et Cosmochimica Acta*, *63*(13–14), 2089–2104. https://doi.org/10.1016/S0016-7037(99)00090-3

Connolly, J. A. D. (1990). Multivariable phase diagrams; an algorithm based on generalized thermodynamics. *American Journal of Science*, *290*(6), 666–718. https://doi.org/10.2475/ajs.290.6.666

Dasgupta, R., Buono, A., Whelan, G., & Walker, D. (2009). High-pressure melting relations in Fe–C–S systems: Implications for formation, evolution, and structure of metallic cores in planetary bodies. *Geochimica et Cosmochimica Acta*, *73*(21), 6678–6691. https://doi.org/10.1016/j.gca.2009.08.001

Dasgupta, R., Chi, H., Shimizu, N., Buono, A. S., & Walker, D. (2013). Carbon solution and partitioning between metallic and silicate melts in a shallow magma ocean: Implications for the origin and distribution of terrestrial carbon. *Geochimica et Cosmochimica Acta*, *102*, 191–212. https://doi.org/10.1016/j.gca.2012.10.011

Defouilloy, C., Cartigny, P., Assayag, N., Moynier, F., & Barrat, J.-A. (2016). High-precision sulfur isotope composition of enstatite meteorites and implications of the formation and evolution of their parent bodies. *Geochimica et Cosmochimica Acta*, *172*, 393–409. https://doi.org/10.1016/j.gca.2015.10.009

Duffy, T., Madhusudhan, N., & Lee, K. K. M. (2015). Mineralogy of super-Earth planets. *Treatise on Geophysics* (2nd ed., Vol. *2*, pp. 149–178). https://doi.org/10.1016/b978-0-444-53802-4.00053-1

Ebel, D., & Stewart, S. (2018). The elusive origin of Mercury. In S. C. Solomon, L. R. Nittler, & B. J. Anderson (Eds.), *Mercury: The view after MESSENGER (Chapter 18)*. Cambridge University Press. https://doi.org/10.1017/9781316650684.019

Ebel, D. S., & Alexander, C. M. O. 'D. (2011). Equilibrium condensation from chondritic porous IDP enriched vapor: Implications for Mercury and enstatite chondrite origins. *Planetary and Space Science*, *59*(15), 1888–1894. https://doi.org/10.1016/j.pss.2011.07.017

Edmund, E., Morard, G., Baron, M. A., Rivoldini, A., Yokoo, S., Boccato, S., et al. (2022). The Fe-FeSi phase diagram at Mercury's core conditions. *Nature Communications*, *13*(1), 387. https://doi.org/10.1038/s41467-022-27991-9

Fegley, B., Jr., & Cameron, A. G. W. (1987). A vaporization model for iron/silicate fractionation in the Mercury protoplanet. *Earth and Planetary Science Letters*, *82*(3–4), 207–222. https://doi.org/10.1016/0012-821x(87)90196-8

Fischer, R. A., Cottrell, E., Hauri, E., Lee, K. K., & Le Voyer, M. (2020). The carbon content of Earth and its core. *Proceedings of the National Academy of Sciences*, *117*(16), 8743–8749. https://doi.org/10.1073/pnas.1919930117

Fischer, R. A., Nakajima, Y., Campbell, A. J., Frost, D. J., Harries, D., Langenhorst, F., et al. (2015). High pressure metal–silicate partitioning of Ni, Co, V, Cr, Si, and O. *Geochimica et Cosmochimica Acta*, *167*, 177–194. https://doi.org/10.1016/j.gca.2015.06.026

Fogel, R. A. (2005). Aubrite basalt vitrophyres: The missing basaltic component and high-sulfur silicate melts. *Geochimica et Cosmochimica Acta*, *69*(6), 1633–1648. https://doi.org/10.1016/j.gca.2003.11.032

Fuhrman, M. L., & Lindsley, D. H. (1988). Ternary-feldspar modeling and thermometry. *American Mineralogist*, *73*(3–4), 201–215.

Genova, A., Goossens, S., Mazarico, E., Lemoine, F. G., Neumann, G. A., Kuang, W., et al. (2019). Geodetic evidence that Mercury has a solid inner core. *Geophysical Research Letters*, *46*(7), 3625–3633. https://doi.org/10.1029/2018GL081135

Gerya, T. (2019). *Introduction to numerical geodynamic modelling*. Cambridge University Press.

Gessmann, C. K., & Wood, B. J. (2002). Potassium in the Earth's core? *Earth and Planetary Science Letters*, *200*(1–2), 63–78. https://doi.org/10.1016/s0012-821x(02)00593-9

Ghiorso, M. S., & Sack, R. O. (1995). Chemical mass transfer in magmatic processes IV. A revised and internally consistent thermodynamic model for the interpolation and extrapolation of liquid-solid equilibria in magmatic systems at elevated temperatures and pressures. *Contributions to Mineralogy and Petrology*, *119*(2–3), 197–212. https://doi.org/10.1007/BF00307281

Goettel, K. A. (1988). Present bounds on the bulk composition of Mercury - Implications for planetary formation processes. In F. Vilas, C. R. Chapman, & M. S. Matthews (Eds.), *Mercury* (pp. 613–621). The University of Arizona Press.

Grady, M. M., & Pillinger, C. T. (1990). ALH 85085: Nitrogen isotope analysis of a highly unusual primitive chondrite. *Earth and Planetary Science Letters*, *97*(1–2), 29–40. https://doi.org/10.1016/0012-821X(90)90096-G

Grasset, O., Sotin, C., & Deschamps, F. (2000). On the internal structure and dynamics of Titan. *Planetary and Space Science*, *48*(7–8), 617–636. https://doi.org/10.1016/s0032-0633(00)00039-8

Green, D. H., & Ringwood, A. E. (1967). The stability fields of aluminous pyroxene peridotite and garnet peridotite and their relevance in upper mantle structure. *Earth and Planetary Science Letters*, *3*, 151–160. https://doi.org/10.1016/0012-821X(67)90027-1

Hansen, L. N., & Warren, J. M. (2015). Quantifying the effect of pyroxene on deformation of peridotite in a natural shear zone. *Journal of Geophysical Research: Solid Earth*, *120*(4), 2717–2738. https://doi.org/10.1002/2014jb011584

Hauck, S. A., Margot, J. L., Solomon, S. C., Phillips, R. J., Johnson, C. L., Lemoine, F. G., et al. (2013). The curious case of Mercury's internal structure. *Journal of Geophysical Research: Planets*, *118*(6), 1204–1220. https://doi.org/10.1002/jgre.20091

Heinrich, C. A., & Connolly, J. A. D. (2022). Physical transport of magmatic sulfides promotes copper enrichment in hydrothermal ore fluids. *Geology*, *50*(10), 1101–1105. https://doi.org/10.1130/G50138.1

Hier-Majumder, S., Mei, S., & Kohlstedt, D. L. (2005). Water weakening of clinopyroxenite in diffusion creep. *Journal of Geophysical Research*, *110*(B7), B07406. https://doi.org/10.1029/2004jb003414

Hinkel, N. R., Timmes, F. X., Young, P. A., Pagano, M. D., & Turnbull, M. C. (2014). Stellar abundances in the solar neighborhood: The Hypatia Catalog. *The Astronomical Journal*, *148*(3), 54. https://doi.org/10.1088/0004-6256/148/3/54

Hinkel, N. R., & Unterborn, C. T. (2018). The star–planet connection. I. Using stellar composition to observationally constrain planetary mineralogy for the 10 closest stars. *The Astrophysical Journal*, *853*(1), 83. https://doi.org/10.3847/1538-4357/aaa5b4

Hinkel, N. R., Young, P. A., Pagano, M. D., Desch, S. J., Anbar, A. D., Adibekyan, V., et al. (2016). A comparison of stellar elemental abundance techniques and measurements. *The Astrophysical Journal - Supplement Series*, *226*(1), 4. https://doi.org/10.3847/0067-0049/226/1/4

Hirose, K., Morard, G., Sinmyo, R., Umemoto, K., Hernlund, J., Helffrich, G., & Labrosse, S. (2017). Crystallization of silicon dioxide and compositional evolution of the Earth's core. *Nature*, *543*(7643), 99–102. https://doi.org/10.1038/nature21367

Hirschmann, M. M., & Stolper, E. M. (1996). A possible role for garnet pyroxenite in the origin of the "garnet signature" in MORB. *Contributions to Mineralogy and Petrology*, *124*(2), 185–208. https://doi.org/10.1007/s004100050184

Hitchings, R. S., Paterson, M. S., & Bitmead, J. (1989). Effects of iron and magnetite additions in olivine-pyroxene rheology. *Physics of the Earth and Planetary Interiors*, *55*(3–4), 277–291. https://doi.org/10.1016/0031-9201(89)90076-9

Holland, T., & Powell, R. (2003). Activity–composition relations for phases in petrological calculations: An asymmetric multicomponent formulation. *Contributions to Mineralogy and Petrology*, *145*(4), 492–501. https://doi.org/10.1007/s00410-003-0464-z

Holland, T. J., Green, E. C., & Powell, R. (2018). Melting of peridotites through to granites: A simple thermodynamic model in the system KNCFMASHTOCr. *Journal of Petrology*, *59*(5), 881–900. https://doi.org/10.1093/petrology/egy048

Holland, T. J. B., & Powell, R. (2011). An improved and extended internally consistent thermodynamic dataset for phases of petrological interest, involving a new equation of state for solids [Dataset]. *Journal of Metamorphic Geology*, *29*(3), 333–383. https://doi.org/10.1111/j.1525-1314.2010.00923

Holzheid, A., & Grove, T. L. (2002). Sulfur saturation limits in silicate melts and their implications for core formation scenarios for terrestrial planets. *American Mineralogist*, *87*(2–3), 227–237. https://doi.org/10.2138/am-2002-2-304

Hutchison, R. (2004). *Meteorites: A petrologic, chemical, and isotopic synthesis*. Cambridge University Press.

Ivanova, M. A., Kononkova, N. N., Franchi, I. A., Verchovsky, A. B., Korochantseva, E. V., Trieloff, M., et al. (2006). Isheyevo Meteorite: Genetic link between CH and CB chondrites? In *Paper presented at 37th Lunar and Planetary Science Conference, Houston, Texas*.

Jarosewich, E. (1990). Chemical analyses of meteorites: A compilation of stony and iron meteorite analyses. *Meteoritics*, *25*(4), 323–337. https://doi.org/10.1111/j.1945-5100.1990.tb00717.x

Javoy, M., Kaminski, E., Guyot, F., Andrault, D., Sanloup, C., Moreira, M., et al. (2010). The chemical composition of the Earth: Enstatite chondrite models. *Earth and Planetary Science Letters*, *293*(3–4), 259–268. https://doi.org/10.1016/j.epsl.2010.02.033

Jennings, E. S., & Holland, T. J. (2015). A simple thermodynamic model for melting of peridotite in the system NCFMASOCr. *Journal of Petrology*, *56*(5), 869–892. https://doi.org/10.1093/petrology/egv020

Ji, S., Wang, Z., & Wirth, R. (2001). Bulk flow strength of forsterite–enstatite composites as a function of forsterite content. *Tectonophysics*, *341*(1–4), 69–93. https://doi.org/10.1016/S0040-1951(01)00191-3

Kallemeyn, G. W., & Wasson, J. T. (1986). Compositions of enstatite (EH3, EH4, 5 and EL6) chondrites: Implications regarding their formation. *Geochimica et Cosmochimica Acta*, *50*(10), 2153–2164. https://doi.org/10.1016/0016-7037(86)90070-0

Keil, K. (1968). Mineralogical and chemical relationships among enstatite chondrites. *Journal of Geophysical Research*, *73*(22), 6945–6976. https://doi.org/10.1029/JB073i022p06945

Keil, K. (2010). Enstatite achondrite meteorites (aubrites) and the histories of their asteroidal parent bodies. *Geochemistry*, *70*(4), 295–317. https://doi.org/10.1016/j.chemer.2010.02.002

Keppler, H., & Golabek, G. (2019). Graphite floatation on a magma ocean and the fate of carbon during core formation. *Geochemical Perspectives Letters*, *11*, 12–17. https://doi.org/10.7185/geochemlet.1918

Kilburn, M. R., & Wood, B. J. (1997). Metal–silicate partitioning and the incompatibility of S and Si during core formation. *Earth and Planetary Science Letters*, *152*(1–4), 139–148. https://doi.org/10.1016/S0012-821X(97)00125-8

Kirby, S. H., & Kronenberg, A. K. (1987). Rheology of the lithosphere: Selected topics. *Reviews of Geophysics*, *25*(6), 1219–1244. https://doi.org/10.1029/RG025i006p01219

Knibbe, J. S., Rivoldini, A., Luginbuhl, S. M., Namur, O., Charlier, B., Mezouar, M., et al. (2021). Mercury's interior structure constrained by density and P-wave velocity measurements of liquid Fe-Si-C alloys. *Journal of Geophysical Research: Planets*, *126*(1), e2020JE006651. https://doi.org/10.1029/2020JE006651

Knibbe, J. S., & Van Hoolst, T. (2021). Modelling of thermal stratification at the top of a planetary core: Application to the cores of Earth and Mercury and the thermal coupling with their mantles. *Physics of the Earth and Planetary Interiors*, *321*, 106804. https://doi.org/10.1016/j.pepi.2021.106804

Knibbe, J. S., & van Westrenen, W. (2015). The interior configuration of planet Mercury constrained by moment of inertia and planetary contraction. *Journal of Geophysical Research: Planets*, *120*(11), 1904–1923. https://doi.org/10.1002/2015JE004908

Knibbe, J. S., & van Westrenen, W. (2018). The thermal evolution of Mercury's Fe–Si core. *Earth and Planetary Science Letters*, *482*, 147–159. https://doi.org/10.1016/j.epsl.2017.11.006

Kohlstedt, D. L., Evans, B., & Mackwell, S. J. (1995). Strength of the lithosphere: Constraints imposed by laboratory experiments. *Journal of Geophysical Research*, *100*(B9), 17587–17602. https://doi.org/10.1029/95JB01460

Kruijer, T. S., Kleine, T., & Borg, L. E. (2020). The great isotopic dichotomy of the early Solar System. *Nature Astronomy*, *4*(1), 32–40. https://doi.org/10.1038/s41550-019-0959-9

Kuskov, O. L., & Kronrod, V. A. (2005). Internal structure of Europa and Callisto. *Icarus*, *177*(2), 550–569. https://doi.org/10.1016/j.icarus.2005.04.014

Labrosse, S. (2003). Thermal and magnetic evolution of the Earth's core. *Physics of the Earth and Planetary Interiors*, *140*(1–3), 127–143. https://doi.org/10.1016/j.pepi.2003.07.006

Lambart, S., Baker, M. B., & Stolper, E. M. (2016). The role of pyroxenite in basalt genesis: Melt-PX, a melting parameterization for mantle pyroxenites between 0.9 and 5 GPa. *Journal of Geophysical Research: Solid Earth*, *121*(8), 5708–5735. https://doi.org/10.1002/2015JB012762

Lambart, S., Laporte, D., Provost, A., & Schiano, P. (2012). Fate of pyroxenite-derived melts in the peridotitic mantle: Thermodynamic and experimental constraints. *Journal of Petrology*, *53*(3), 451–476. https://doi.org/10.1093/petrology/egr068

Lambart, S., Laporte, D., & Schiano, P. (2009). An experimental study of pyroxenite partial melts at 1 and 1.5 GPa: Implications for the major-element composition of Mid-Ocean Ridge Basalts. *Earth and Planetary Science Letters*, *288*(1–2), 335–347. https://doi.org/10.1016/j.epsl.2009.09.03

Lark, L. H., Head, J. W., & Huber, C. (2023). Evidence for a carbon-rich Mercury from the distribution of low-reflectance material (LRM) associated with large impact basins. *Earth and Planetary Science Letters*, *613*, 118192. https://doi.org/10.1016/j.epsl.2023.118192

Lark, L. H., Parman, S., Huber, C., Parmentier, E. M., & Head III, J. W. (2022). Sulfides in Mercury's mantle: Implications for Mercury's interior as interpreted from moment of inertia. *Geophysical Research Letters*, *49*(6), e2021GL096713. https://doi.org/10.1029/2021GL096713

Lawlis, J. D. (1998). *High temperature creep of synthetic olivine-enstatite aggregates* (Doctoral dissertation). Pennsylvania State University.

Le Maitre, R. W., Streckeisen, A., Zanettin, B., Le Bas, M. J., Bonin, B., & Bateman, P. (Eds.). (2002). *Igneous rocks: A classification and glossary of terms: recommendations of the International Union of Geological Sciences Subcommission on the Systematics of Igneous Rocks*. Cambridge University Press.

Li, Y., Dasgupta, R., & Tsuno, K. (2015). The effects of sulfur, silicon, water, and oxygen fugacity on carbon solubility and partitioning in Fe-rich alloy and silicate melt systems at 3 GPa and 1600 C: Implications for core–mantle differentiation and degassing of magma oceans and reduced planetary mantles. *Earth and Planetary Science Letters*, *415*, 54–66. https://doi.org/10.1016/j.epsl.2015.01.017

Litasov, K. D., & Shatskiy, A. F. (2016). Composition of the Earth's core: A review. *Russian Geology and Geophysics*, *57*(1), 22–46. https://doi.org/10.1016/j.rgg.2016.01.003

Lodders, K., Palme, H., & Wlotzka, F. (1993). Trace elements in mineral separates of the Pena Blanca Spring aubrite: Implications for the evolution of the aubrite parent body. *Meteoritics*, *28*(4), 538–551. https://doi.org/10.1111/j.1945-5100.1993.tb00277.x

Mackwell, S. J. (1991). High-temperature rheology of enstatite: Implications for creep in the mantle. *Geophysical Research Letters*, *18*(11), 2027–2030. https://doi.org/10.1029/91GL02492

Malavergne, V., Berthet, S., & Righter, K. (2007). Formation of CaS-MgS in enstatite chondrites and achondrites as a function of redox conditions and temperature: Constraints on their evolution in a planetesimal and in a proto-planet. In *Lunar and Planetary Science Conference*.

Malavergne, V., Cordier, P., Righter, K., Brunet, F., Zanda, B., Addad, A., et al. (2014). How Mercury can be the most reduced terrestrial planet and still store iron in its mantle. *Earth and Planetary Science Letters*, *394*, 186–197. https://doi.org/10.1016/j.epsl.2014.03.028

Malavergne, V., Tarrida, M., Combes, R., Bureau, H., Jones, J., & Schwandt, C. (2007). New high-pressure and high-temperature metal/silicate partitioning of U and Pb: Implications for the cores of the Earth and Mars. *Geochimica et Cosmochimica Acta*, *71*(10), 2637–2655. https://doi.org/10.1016/j.gca.2007.03.011

Malavergne, V., Toplis, M. J., Berthet, S., & Jones, J. (2010). Highly reducing conditions during core formation on Mercury: Implications for internal structure and the origin of a magnetic field. *Icarus*, *206*(1), 199–209. https://doi.org/10.1016/j.icarus.2009.09.001

Marcy, G. W., & Butler, R. P. (1996). A planetary companion to 70 Virginis. *The Astrophysical Journal*, *464*(2), L147–L151. https://doi.org/10.1086/310096

Margot, J.-L., Hauck, S. A., Mazarico, E., Padovan, S., & Peale, S. J. (2018). Mercury's internal structure. In S. C. Solomon, L. R. Nittler, & B. J. Anderson (Eds.), *Mercury* (1st ed., pp. 85–113). Cambridge University Press.

Mason, B. (1966). The enstatite chondrites. *Geochimica et Cosmochimica Acta*, *30*(1), 23–39. https://doi.org/10.1016/0016-7037(66)90089-5

McCoy, T. J., Dickinson, T. L., & Lofgren, G. E. (1999). Partial melting of the Indarch (EH4) meteorite: A textural, chemical, and phase relations view of melting and melt migration. *Meteoritics & Planetary Science*, *34*(5), 735–746. https://doi.org/10.1111/j.1945-5100.1999.tb01386.x

McCubbin, F. M., Riner, M. A., Vander Kaaden, K. E., & Burkemper, L. K. (2012). Is Mercury a volatile-rich planet? *Geophysical Research Letters*, *39*(9), L09202. https://doi.org/10.1029/2012GL051711

McDonough, W. F., & Yoshizaki, T. (2021). Terrestrial planet compositions controlled by accretion disk magnetic field. *Progress in Earth and Planetary Science*, *8*, 1–12. https://doi.org/10.1186/s40645-021-00429-4

Michel, N. C., Hauck, S. A., Solomon, S. C., Phillips, R. J., Roberts, J. H., & Zuber, M. T. (2013). Thermal evolution of Mercury as constrained by MESSENGER observations. *Journal of Geophysical Research: Planets*, *118*(5), 1033–1044. https://doi.org/10.1002/jgre.20049

Mookherjee, M., Nakajima, Y., Steinle-Neumann, G., Glazyrin, K., Wu, X., Dubrovinsky, L., et al. (2011). High-pressure behavior of iron carbide (Fe_7C_3) at inner core conditions. *Journal of Geophysical Research*, *116*(B4), B04201. https://doi.org/10.1029/2010JB007819

Morgan, J. W., & Anders, E. (1980). Chemical composition of Earth, Venus, and Mercury. *Proceedings of the National Academy of Sciences*, *77*(12), 6973–6977. https://doi.org/10.1073/pnas.77.12.6973

Mueller, S., & McKinnon, W. B. (1988). Three-layered models of Ganymede and Callisto: Compositions, structures, and aspects of evolution. *Icarus*, *76*(3), 437–464. https://doi.org/10.1016/0019-1035(88)90014-0

Nakagawa, T., & Tackley, P. J. (2004a). Effects of thermo-chemical mantle convection on the thermal evolution of the Earth's core. *Earth and Planetary Science Letters*, *220*(1–2), 107–119. https://doi.org/10.1016/S0012-821X(04)00055-X

Nakagawa, T., & Tackley, P. J. (2004b). Thermo-chemical structure in the mantle arising from a three-component convective system and implications for geochemistry. *Physics of the Earth and Planetary Interiors*, *146*(1–2), 125–138. https://doi.org/10.1016/j.pepi.2003.05.006

Namur, O., Charlier, B., Holtz, F., Cartier, C., & McCammon, C. (2016). Sulfur solubility in reduced mafic silicate melts: Implications for the speciation and distribution of sulfur on Mercury. *Earth and Planetary Science Letters*, *448*, 102–114. https://doi.org/10.1016/j.epsl.2016.05.024

Namur, O., Collinet, M., Charlier, B., Grove, T. L., Holtz, F., & McCammon, C. (2016). Melting processes and mantle sources of lavas on Mercury. *Earth and Planetary Science Letters*, *439*, 117–128. https://doi.org/10.1016/j.epsl.2016.01.030

Néri, A., Guyot, F., Reynard, B., & Sotin, C. (2020). A carbonaceous chondrite and cometary origin for icy moons of Jupiter and Saturn. *Earth and Planetary Science Letters*, *530*, 115920. https://doi.org/10.1016/j.epsl.2019.115920

Nittler, L. R., Chabot, N. L., Grove, T. L., & Peplowski, P. N. (2018). The chemical composition of Mercury. In S. C. Solomon, L. R. Nittler, & B. J. Anderson (Eds.), *Mercury: The View after MESSENGER* (1st ed., pp. 30–51). Cambridge University Press.

Nittler, L. R., Starr, R. D., Weider, S. Z., McCoy, T. J., Boynton, W. V., Ebel, D. S., et al. (2011). The major-element composition of Mercury's surface from MESSENGER X-ray spectrometry. *Science*, *333*(6051), 1847–1850. https://doi.org/10.1126/science.1211567

Ohuchi, T., Karato, S., & Fujino, K. (2011). Strength of single-crystal orthopyroxene under lithospheric conditions. *Contributions to Mineralogy and Petrology*, *161*(6), 961–975. https://doi.org/10.1007/s00410-010-0574-3

Olson, P., Deguen, R., Rudolph, M. L., & Zhong, S. (2015). Core evolution driven by mantle global circulation. *Physics of the Earth and Planetary Interiors*, *243*, 44–55. https://doi.org/10.1016/j.pepi.2015.03.002

Padovan, S., Tosi, N., Plesa, A. C., & Ruedas, T. (2017). Impact-induced changes in source depth and volume of magmatism on Mercury and their observational signatures. *Nature Communications*, *8*(1), 1945. https://doi.org/10.1038/s41467-017-01692-0

Perryman, M. A. C. (2011). *The exoplanet handbook*. Cambridge University Press.

Pertermann, M., & Hirschmann, M. M. (2003). Partial melting experiments on a MORB-like pyroxenite between 2 and 3 GPa: Constraints on the presence of pyroxenite in basalt source regions from solidus location and melting rate. *Journal of Geophysical Research*, *108*(B2), 2125. https://doi.org/10.1029/2000JB000118

Philpotts, A. R., & Ague, J. J. (2022). *Principles of igneous and metamorphic petrology*. Cambridge University Press.

Pirotte, H., Cartier, C., Namur, O., Pommier, A., Zhang, Y., Berndt, J., et al. (2023). Internal differentiation and volatile budget of Mercury inferred from the partitioning of heat-producing elements at highly reduced conditions. *Icarus*, *405*, 115699. https://doi.org/10.1016/j.icarus.2023.115699

Putirka, K. D., & Rarick, J. C. (2019). The composition and mineralogy of rocky exoplanets: A survey of> 4000 stars from the Hypatia Catalog. *American Mineralogist: Journal of Earth and Planetary Materials*, *104*(6), 817–829. https://doi.org/10.2138/am-2019-6787

Putirka, K. D., & Xu, S. (2021). Polluted white dwarfs reveal exotic mantle rock types on exoplanets in our solar neighborhood. *Nature Communications*, *12*(1), 6168. https://doi.org/10.1038/s41467-021-26403-8

Raleigh, C. B., Kirby, S. H., Carter, N. L., & Ave' Lallemant, H. G. (1971). Slip and the clinoenstatite transformation as competing rate processes in enstatite. *Journal of Geophysical Research*, *76*(17), 4011–4022. https://doi.org/10.1029/jb076i017p04011

Ranalli, G. (1995). *Rheology of the Earth*. Springer Science & Business Media.

Ranalli, G. (1997). Rheology of the lithosphere in space and time. *Geological Society, London, Special Publications*, *121*(1), 19–37. https://doi.org/10.1144/GSL.SP.1997.121.01.02

Redmond, H. L., & King, S. D. (2007). Does mantle convection currently exist on Mercury? *Physics of the Earth and Planetary Interiors*, *164*(3–4), 221–231. https://doi.org/10.1016/j.pepi.2007.07.004

Righter, K., Herd, C. D., & Boujibar, A. (2020). Redox Processes in early earth accretion and in terrestrial bodies. Elements: An International Magazine of Mineralogy. *Geochemistry, and Petrology*, *16*(3), 161–166. https://doi.org/10.2138/gselements.16.3.161

Riner, M. A., Bina, C. R., Robinson, M. S., & Desch, S. J. (2008). Internal structure of Mercury: Implications of a molten core. *Journal of Geophysical Research*, *113*(E8), E08013. https://doi.org/10.1029/2007JE002993

Rivoldini, A., & Van Hoolst, T. (2013). The interior structure of Mercury constrained by the low-degree gravity field and the rotation of Mercury. *Earth and Planetary Science Letters*, *377*, 62–72. https://doi.org/10.1016/j.epsl.2013.07.021

Rivoldini, A., Van Hoolst, T., & Verhoeven, O. (2009). The interior structure of Mercury and its core sulfur content. *Icarus*, *201*(1), 12–30. https://doi.org/10.1016/j.icarus.2008.12.020

Rohrbach, A., Ballhaus, C., Golla–Schindler, U., Ulmer, P., Kamenetsky, V. S., & Kuzmin, D. V. (2007). Metal saturation in the upper mantle. *Nature*, *449*(7161), 456–458. https://doi.org/10.1038/nature06183

Ross, J. V., & Nielsen, K. C. (1978). High-temperature flow of wet polycrystalline enstatite. *Tectonophysics*, *44*(1–4), 233–261. https://doi.org/10.1016/0040-1951(78)90072-0

Rubin, A., & Ma, C. (2021). *Meteorite mineralogy (Cambridge Planetary Science)*. Cambridge University Press.

Rubin, A. E. (1984). The Blithfield meteorite and the origin of sulfide-rich, metal-poor clasts and inclusions in brecciated enstatite chondrites. *Earth and Planetary Science Letters*, *67*(3), 273–283. https://doi.org/10.1016/0012-821X(84)90167-5

Schaefer, L., Jacobsen, S. B., Remo, J. L., Petaev, M. I., & Sasselov, D. D. (2017). Metal-silicate partitioning and its role in core formation and composition on super-Earths. *The Astrophysical Journal*, *835*(2), 234. https://doi.org/10.3847/1538-4357/835/2/234

Schoenbeck, T. W., & Palme, H. (2003). Silicon concentrations in metal grains of CB-, CH and CR-chondrites – Implications for their formation. In *Paper presented at 34th Annual Lunar and Planetary Science Conference. League City, Texas*.

Schoenbeck, T. W., & Palme, H. (2005). SIMS analysis of moderately lithophile elements in CR and CB chondrite metal – Characteristic properties of pristine and processed metal. In *Paper presented at 36th Annual Lunar and Planetary Science Conference. League City, Texas*.

Scott, E. R. (1988). A new kind of primitive chondrite, Allan Hills 85085. *Earth and Planetary Science Letters*, *91*(1–2), 1–18. https://doi.org/10.1016/0012-821X(88)90147-1

Sears, D. W. (1980). Formation of E chondrites and aubrites—A thermodynamic model. *Icarus*, *43*(2), 184–202. https://doi.org/10.1016/0019-1035(80)90120-7

Siebert, J., Badro, J., Antonangeli, D., & Ryerson, F. J. (2012). Metal–silicate partitioning of Ni and Co in a deep magma ocean. *Earth and Planetary Science Letters*, *321*, 189–197. https://doi.org/10.1016/j.epsl.2012.01.013

Smith, D. E., Zuber, M. T., Phillips, R. J., Solomon, S. C., Hauck, S. A., Lemoine, F. G., et al. (2012). Gravity field and internal structure of Mercury from MESSENGER. *Science*, *336*(6078), 214–217. https://doi.org/10.1126/science.1218809

Smith, R. F., Fratanduono, D. E., Braun, D. G., Duffy, T. S., Wicks, J. K., Celliers, P. M., et al. (2018). Equation of state of iron under core conditions of large rocky exoplanets. *Nature Astronomy*, *2*(6), 452–458. https://doi.org/10.1038/s41550-018-0437-9

Smrekar, S. E., Elkins-Tanton, L., Leitner, J. J., Lenardic, A., Mackwell, S., Moresi, L., et al. (2007). Tectonic and thermal evolution of Venus and the role of volatiles: Implications for understanding the terrestrial planets. *Exploring Venus as a Terrestrial Planet*, *176*, 45–71. https://doi.org/10.1029/176gm05

Sotin, C., Jackson, J. M., & Seager, S. (2010). Terrestrial planet interiors. In S. Seager (Ed.), *Exoplanets* (pp. 375–395). University of Arizona.

Steenstra, E. S., Seegers, A. X., Putter, R., Berndt, J., Klemme, S., Matveev, S., et al. (2020). Metal-silicate partitioning systematics of siderophile elements at reducing conditions: A new experimental database. *Icarus*, *335*, 113391. https://doi.org/10.1016/j.icarus.2019.113391

Steenstra, E. S., Trautner, V. T., Berndt, J., Klemme, S., & van Westrenen, W. (2020). Trace element partitioning between sulfide-metal-and silicate melts at highly reduced conditions: Insights into the distribution of volatile elements during core formation in reduced bodies. *Icarus*, *335*, 113408. https://doi.org/10.1016/j.icarus.2019.113408

Steenstra, E. S., & van Westrenen, W. (2020). Geochemical constraints on core-mantle differentiation in Mercury and the aubrite parent body. *Icarus*, *340*, 113621. https://doi.org/10.1016/j.icarus.2020.113621

Steinbrügge, G., Dumberry, M., Rivoldini, A., Schubert, G., Cao, H., Schroeder, D. M., & Soderlund, K. M. (2021). Challenges on Mercury's interior structure posed by the new measurements of its obliquity and tides. *Geophysical Research Letters*, *48*(3), e2020GL089895. https://doi.org/10.1029/2020GL089895

Stixrude, L. (2014). Melting in super-earths. *Philosophical Transactions of the Royal Society A: Mathematical, Physical & Engineering Sciences*, *372*(2014), 20130076. https://doi.org/10.1098/rsta.2013.0076

Stockstill-Cahill, K. R., McCoy, T. J., Nittler, L. R., Weider, S. Z., & Hauck, S. A. (2012). Magnesium-rich crustal compositions on Mercury: Implications for magmatism from petrologic modeling. *Journal of Geophysical Research*, *117*(E12), E00L15. https://doi.org/10.1029/2012je004140

Suer, T. A., Siebert, J., Remusat, L., Menguy, N., & Fiquet, G. (2017). A sulfur-poor terrestrial core inferred from metal–silicate partitioning experiments. *Earth and Planetary Science Letters*, *469*, 84–97. https://doi.org/10.1016/j.epsl.2017.04.016

Tackley, P. J. (2002). Strong heterogeneity caused by deep mantle layering. *Geochemistry, Geophysics, Geosystems*, *3*(4), 1–22. https://doi.org/10.1029/2001GC000167

Taylor, G. J., & Scott, E. R. D. (2001). Workshop on Mercury: Space environment, surface, and interior.

Taylor, G. J., & Scott, E. R. D. (2003). Mercury. In A. M. Davis, H. D. Holland, & K. K. Turekian (Eds.), *Meteorites, Comets, and Planets*, *Treatise on Geochemistry* (Vol. 1, pp. 477–485). Pergamon. https://doi.org/10.1016/b0-08-043751-6/01071-9

Thompson, J. B. (1982). Reaction Space: An algebraic and geometric approach. In J. M. Ferry (Ed.), *Characterization of Metamorphism through mineral equilibria*, *Reviews in mineralogy* (Vol. 10, pp. 33–52). Mineralogical Society of America.

Tosi, N., Grott, M., Plesa, A. C., & Breuer, D. (2013). Thermochemical evolution of Mercury's interior. *Journal of Geophysical Research: Planets*, *118*(12), 2474–2487. https://doi.org/10.1002/jgre.20168

Trønnes, R. G., Baron, M. A., Eigenmann, K. R., Guren, M. G., Heyn, B. H., Løken, A., & Mohn, C. E. (2019). Core formation, mantle differentiation and core-mantle interaction within Earth and the terrestrial planets. *Tectonophysics*, *760*, 165–198. https://doi.org/10.1016/j.tecto.2018.10.021

Udry, A., Wilbur, Z. E., Rahib, R. R., McCubbin, F. M., Vander Kaaden, K. E., McCoy, T. J., et al. (2019). Reclassification of four aubrites as enstatite chondrite impact melts: Potential geochemical analogs for Mercury. *Meteoritics and Planetary Science*, *54*(4), 785–810. https://doi.org/10.1111/maps.13252

Umemoto, K., Wentzcovitch, R. M., & Allen, P. B. (2006). Dissociation of MgSiO$_3$ in the cores of gas giants and terrestrial exoplanets. *Science*, *311*(5763), 983–986. https://doi.org/10.1126/science.1120865

Umemoto, K., Wentzcovitch, R. M., Wu, S., Ji, M., Wang, C. Z., & Ho, K. M. (2017). Phase transitions in MgSiO$_3$ post-perovskite in super-Earth mantles. *Earth and Planetary Science Letters*, *478*, 40–45. https://doi.org/10.1016/j.epsl.2017.08.032

Unterborn, C. T., Desch, S. J., Haldemann, J., Lorenzo, A., Schulze, J. G., Hinkel, N. R., & Panero, W. R. (2023). The nominal ranges of rocky planet masses, radii, surface gravities, and bulk densities. *The Astrophysical Journal*, *944*(1), 42. https://doi.org/10.3847/1538-4357/acaa3b

Unterborn, C. T., & Panero, W. R. (2019). The pressure and temperature limits of likely rocky exoplanets. *Journal of Geophysical Research: Planets*, *124*(7), 1704–1716. https://doi.org/10.1029/2018JE005844

Valencia, D. (2013). Composition and internal dynamics of super-Earths. *Physics and Chemistry of the Deep Earth*, 271–294. https://doi.org/10.1002/9781118529492.ch9

Valencia, D., O'Connell, R. J., & Sasselov, D. (2006). Internal structure of massive terrestrial planets. *Icarus*, *181*(2), 545–554. https://doi.org/10.1016/j.icarus.2005.11.021

Vander Kaaden, K. E., & McCubbin, F. M. (2015). Exotic crust formation on Mercury: Consequences of a shallow, FeO-poor mantle. *Journal of Geophysical Research: Planets*, *120*(2), 195–209. https://doi.org/10.1002/2014JE004733

Vander Kaaden, K. E., & McCubbin, F. M. (2016). The origin of boninites on Mercury: An experimental study of the northern volcanic plains lavas. *Geochimica et Cosmochimica Acta*, *173*, 246–263. https://doi.org/10.1016/j.gca.2015.10.016

Vander Kaaden, K. E., McCubbin, F. M., Nittler, L. R., Peplowski, P. N., Weider, S. Z., Frank, E. A., & McCoy, T. J. (2017). Geochemistry, mineralogy, and petrology of boninitic and komatiitic rocks on the mercurian surface: Insights into the mercurian mantle. *Icarus*, *285*, 155–168. https://doi.org/10.1016/j.icarus.2016.11.041

Vander Kaaden, K. E., McCubbin, F. M., Turner, A. A., & Ross, D. K. (2020). Constraints on the abundances of carbon and silicon in Mercury's core from experiments in the Fe-Si-C system. *Journal of Geophysical Research: Planets*, *125*(5), e2019JE006239. https://doi.org/10.1029/2019JE006239

Wadhwa, M. (2008). Redox conditions on small bodies, the Moon and Mars. *Reviews in Mineralogy and Geochemistry*, *68*(1), 493–510. https://doi.org/10.2138/rmg.2008.68.17

Wänke, H., Dreibus, G., & Jagoutz, E. (1984). Mantle chemistry and accretion history of the Earth. In *Archaean geochemistry: The origin and evolution of the Archaean Continental crust* (pp. 1–24). Springer Berlin Heidelberg.

Warren, P. H. (2011). Stable-isotopic anomalies and the accretionary assemblage of the Earth and Mars: A subordinate role for carbonaceous chondrites. *Earth and Planetary Science Letters*, *311*(1–2), 93–100. https://doi.org/10.1016/j.epsl.2011.08.047

Wasson, J. T., & Kallemeyn, G. W. (1990). Allan Hills 85085: A subchondritic meteorite of mixed nebular and regolithic heritage. *Earth and Planetary Science Letters*, *101*(2–4), 148–161. https://doi.org/10.1016/0012-821X(90)90150-V

Weider, S. Z., Nittler, L. R., Starr, R. D., Crapster-Pregont, E. J., Peplowski, P. N., Denevi, B. W., et al. (2015). Evidence for geochemical terranes on Mercury: Global mapping of major elements with MESSENGER's X-Ray Spectrometer. *Earth and Planetary Science Letters*, *416*, 109–120. https://doi.org/10.1016/j.epsl.2015.01.023

Weider, S. Z., Nittler, L. R., Starr, R. D., McCoy, T. J., & Solomon, S. C. (2014). Variations in the abundance of iron on Mercury's surface from MESSENGER X-Ray Spectrometer observations. *Icarus*, *235*, 170–186. https://doi.org/10.1016/j.icarus.2014.03.002

Weider, S. Z., Nittler, L. R., Starr, R. D., McCoy, T. J., Stockstill-Cahill, K. R., Byrne, P. K., et al. (2012). Chemical heterogeneity on Mercury's surface revealed by the MESSENGER X-Ray Spectrometer. *Journal of Geophysical Research*, *117*(E12), E00L05. https://doi.org/10.1029/2012JE004153

Weisberg, M. K., & Kimura, M. (2012). The unequilibrated enstatite chondrites. *Geochemistry*, *72*(2), 101–115. https://doi.org/10.1016/j.chemer.2012.04.003

Weisberg, M. K., Prinz, M., Clayton, R. N., Mayeda, T. K., Sugiura, N., & Zashu, S. (1998). The bencubbinite (B) group of the CR clan. *Meteoritics & Planetary Science*, *33*, A166.

Weisberg, M. K., Prinz, M., Clayton, R. N., Mayeda, T. K., Sugiura, N., Zashu, S., & Ebihara, M. (2001). A new metal-rich chondrite grouplet. *Meteoritics & Planetary Science*, *36*(3), 401–418. https://doi.org/10.1111/j.1945-5100.2001.tb01882.x

Weisberg, M. K., Prinz, M., & Nehru, C. E. (1988). Petrology of ALH85085: A chondrite with unique characteristics. *Earth and Planetary Science Letters*, *91*(1–2), 19–32. https://doi.org/10.1016/0012-821X(88)90148-3

White, W. (2013). *Geochemistry* (1st ed.). Wiley.

Wicks, J. K., Smith, R. F., Fratanduono, D. E., Coppari, F., Kraus, R. G., Newman, M. G., et al. (2018). Crystal structure and equation of state of Fe-Si alloys at super-Earth core conditions. *Science Advances*, *4*(4), eaao5864. https://doi.org/10.1126/sciadv.aao5864

Wilbur, Z. E., Udry, A., McCubbin, F. M., vander Kaaden, K. E., DeFelice, C., Ziegler, K., et al. (2022). The effects of highly reduced magmatism revealed through aubrites. *Meteoritics & Planetary Science*, *57*(7), 1387–1420. https://doi.org/10.1111/maps.13823

Wohlers, A., & Wood, B. J. (2015). A Mercury-like component of early Earth yields uranium in the core and high mantle ^{142}Nd. *Nature*, *520*(7547), 337–340. https://doi.org/10.1038/nature14350

Wolszczan, A., & Frail, D. A. (1992). A planetary system around the millisecond pulsar PSR1257+ 12. *Nature*, *355*(6356), 145–147. https://doi.org/10.1038/355145a0

Wood, B. J. (1993). Carbon in the core. *Earth and Planetary Science Letters*, *117*(3–4), 593–607. https://doi.org/10.1016/0012-821x(93)90105-i

Wood, B. J., Li, J., & Shahar, A. (2013). Carbon in the core: Its influence on the properties of core and mantle. *Reviews in Mineralogy and Geochemistry*, *75*(1), 231–250. https://doi.org/10.2138/rmg.2013.75.8

Yamamoto, J., Ando, J. I., Kagi, H., Inoue, T., Yamada, A., Yamazaki, D., & Irifune, T. (2008). In situ strength measurements on natural upper-mantle minerals. *Physics and Chemistry of Minerals*, *35*(5), 249–257. https://doi.org/10.1007/s00269-008-0218-6

Yamamoto, J., Kagi, H., Kaneoka, I., Lai, Y., Prikhod'ko, V. S., & Arai, S. (2002). Fossil pressures of fluid inclusions in mantle xenoliths exhibiting rheology of mantle minerals: Implications for the geobarometry of mantle minerals using micro Raman spectroscopy. *Earth and Planetary Science Letters*, *198*(3–4), 511–519. https://doi.org/10.1016/s0012-821x(02)00528-9

Yasuda, A., Fujii, T., & Kurita, K. (1994). Melting phase relations of an anhydrous mid-ocean ridge basalt from 3 to 20 GPa: Implications for the behavior of subducted oceanic crust in the mantle. *Journal of Geophysical Research*, *99*(B5), 9401–9414. https://doi.org/10.1029/93JB03205

Yaxley, G. M., & Green, D. H. (1998). Reactions between eclogite and peridotite: Mantle refertilisation by subduction of oceanic crust. *Schweizerische mineralogische und petrographische Mitteilungen*, *78*(2), 243–255.

Yokoo, S., Edmund, E., Morard, G., Anna Baron, M., Boccato, S., Decremps, F., et al. (2023). Composition-dependent thermal equation of state of B2 Fe-Si alloys at high pressure. *American Mineralogist*, *108*(3), 536–542. https://doi.org/10.2138/am-2022-8067

Yoshizaki, T., & McDonough, W. F. (2020). The composition of Mars. *Geochimica et Cosmochimica Acta*, *273*, 137–162. https://doi.org/10.1016/j.gca.2020.01.011

Zhang, G., Mei, S., Song, M., & Kohlstedt, D. L. (2017). Diffusion creep of enstatite at high pressures under hydrous conditions. *Journal of Geophysical Research: Solid Earth*, *122*(10), 7718–7728. https://doi.org/10.1002/2017JB014400

Zolotov, M. Y., Sprague, A. L., Hauck, S. A., Nittler, L. R., Solomon, S. C., & Weider, S. Z. (2013). The redox state, FeO content, and origin of sulfur-rich magmas on Mercury. *Journal of Geophysical Research: Planets*, *118*(1), 138–146. https://doi.org/10.1029/2012JE004274